Hallmarks of *Alpha-* and *Betacoronavirus* non-structural protein 7+8 complexes

Boris Krichel[1], Ganesh Bylapudi[2], Christina Schmidt[3], Clement Blanchet[4], Robin Schubert[3], Lea Brings[3], Martin Koehler[5], Renato Zenobi[5], Dmitri Svergun[4], Kristina Lorenzen[3], Ramakanth Madhugiri[2], John Ziebuhr[2], Charlotte Uetrecht[1,3]*

[1]Heinrich Pette Institute, Leibniz Institute for Experimental Virology, Hamburg, Germany;

[2] Institute of Medical Virology, Justus Liebig University Giessen, Giessen, Germany;

[3]European XFEL GmbH, Schenefeld, Germany;

[4]EMBL Hamburg c/o DESY, Notkestraße 85, 22607 Hamburg, Germany

[5]ETH Zurich D-CHAB Lab of Organic Chemistry, Zürich, Switzerland;

*correspondence to charlotte.uetrecht@xfel.eu

Abstract

Coronaviruses infect many different species including humans. The last two decades have seen three zoonotic coronaviruses with SARS-CoV-2 causing a pandemic in 2020. Coronaviral non-structural proteins (nsp) built up the replication-transcription complex (RTC). Nsp7 and nsp8 interact with and regulate the RNA-dependent RNA-polymerase and other enzymes in the RTC. However, the structural plasticity of nsp7+8 complex has been under debate. Here, we present the framework of nsp7+8 complex stoichiometry and topology based on a native mass spectrometry and complementary biophysical techniques of nsp7+8 complexes from seven coronaviruses in the genera *Alpha-* and *Betacoronavirus* including SARS-CoV-2. Their complexes cluster into three groups, which systematically form either heterotrimers or heterotetramers or both, exhibiting distinct topologies. Moreover, even at high protein concentrations mainly heterotetramers are observed for SARS-CoV-2

26 nsp7+8. From these results, the different assembly paths can be pinpointed to specific
27 residues and an assembly model is proposed.

28 **Introduction**

29 Seven coronaviruses (CoV) from six coronavirus species are known to cause infections in
30 humans. While four of these viruses (HCoV-229E, HCoV-NL63, HCoV-OC43, HCoV-HKU1)
31 predominantly cause seasonal outbreaks of (upper) respiratory tract infections with mild
32 disease symptoms in most cases, three other coronaviruses (SARS-CoV, MERS-CoV and
33 SARS-CoV-2) of recent zoonotic origin are associated with lower respiratory tract disease
34 including acute respiratory distress syndrome (ARDS) [1-3]. SARS-CoV-2 is the etiologic
35 agent of COVID-19, a respiratory disease with a wide spectrum of clinical presentations and
36 outcomes. First detected in December 2019, it quickly became pandemic with numbers still
37 growing (>30 million confirmed cases, >1,000,000 deaths, by end September 2020) [4-6].
38 COVID-19 caused major perturbations of historical dimensions in politics, economics and
39 healthcare. Moreover, coronaviruses are important, widespread animal pathogens as
40 illustrated by feline intestine peritonitis virus (FIPV) causing a severe and often fatal disease
41 in cats [7] or porcine coronaviruses [8], such as transmissible-gastroenteritis virus (TGEV) or
42 porcine epidemic diarrhea virus (PEDV), the latter causing massive outbreaks and economic
43 losses in swine industry.

44 The viral replication machinery is largely conserved across the different coronavirus species
45 from the four currently recognized genera *Alpha-*, *Beta-*, *Gamma-* and *Deltacoronavirus*
46 (subfamily *Orthocoronavirinae*, family *Coronaviridae*) [9]. The key components are generally
47 referred to as nonstructural proteins (nsp) and encoded by the viral replicase genes (ORFs 1a
48 and 1b) and translated as parts of the replicase polyproteins pp1a (nsp1-11) or pp1ab (nsp1-
49 16). Translation of the ORF1b-encoded C-terminal part of pp1ab requires a ribosomal (-1)-
50 frameshift immediately upstream of the ORF1a stop codon. Two proteases called PL_{pro} (one
51 or two protease domains in nsp3) and M_{pro} (also called $3CL_{pro}$ or nsp5) facilitate polyprotein
52 processing into 16 (sometimes 15) mature nsps. The majority of these nsps form a membrane-
53 anchored, highly dynamic protein-RNA machinery, the replication-transcription complex
54 (RTC), which mediates replication of the ~30 kb single-strand (+)-sense RNA genome and
55 production of subgenomic mRNAs [9, 10].

56 The main CoV-RTC building block is the fastest known RNA-dependent RNA-polymerase
57 (RdRp) residing in the nsp12 C-terminal domain [11]. For RdRp activity, nsp12 requires
58 binding to its cofactors nsp7 and nsp8 [12]. Recently, high-resolution structures illuminated
59 two binding sites at nsp12, the first for an nsp7+8 (1:1) heterodimer and the second for a
60 single nsp8 [13-16]. For *in vitro* RdRp activity assays, different methods were used to
61 assemble the polymerase complex [11, 17, 18]. So far, the highest processivity *in vitro* was
62 obtained by mixing nsp12 with a flexibly linked nsp7L8 fusion protein.

63 Recently, we reported that SARS-CoV nsp7 and nsp8 form a heterotetramer (2:2) in solution,
64 in which nsp7 subunits have no self-interaction and rather sandwich an nsp8 scaffold with
65 putative head-to-tail interactions [19]. Current knowledge of full-length nsp7+8 complexes is
66 mainly based on two X-ray crystal structures, each of which displays a different quaternary
67 conformation. First, a SARS-CoV nsp7+8 (8:8) hexadecamer is assembled from four (2:2)
68 heterotetramers with similar topologies but two distinct conformations, T1 and T2, which are
69 both consistent with our in solution structure [19] [20]. Second, in a feline coronavirus (FIPV)
70 nsp7+8 (2:1) heterotrimer, nsp8 is associated to two nsp7 molecules that self-interact [21].
71 Moreover, structures of SARS-CoV and SARS-CoV-2 with *N*-terminally truncated forms of
72 nsp8, thus lacking the self-interaction domain, revealed heterotetrameric nsp7+8 complexes
73 around an nsp7 scaffold [22, 23].

74 Current knowledge of coronavirus nsp7+8 complexes suggests a remarkable architectural
75 plasticity but is unsupportive of deducing common principles of complex formation.
76 Moreover, it is unknown if the quaternary structure of nsp7+8 is conserved within a given
77 coronavirus species or between genera. To fill these knowledge gaps, we analyzed nsp7+8
78 complexes derived from seven viruses of the *Alpha*- and *Betacoronavirus* genera, including a
79 range of human coronaviruses, namely SARS-CoV, SARS-CoV-2, MERS-CoV and HCoV-
80 229E (Table S 2). We used native mass spectrometry (MS) to illustrate the landscape of
81 nsp7+8 complexes *in vacuo*, collision induced dissociation tandem MS (CID-MS/MS) to
82 reconstruct complex topology and complementary methods to verify the results [24, 25]. Our
83 findings reveal distinct sets of nsp7+8 complexes for the different CoV species. The results
84 hint at the properties that lead to complex heterogeneity and suggest common principles of
85 complex formation based on two conserved binding sites.

Experimental Results

Native MS illustrates the landscape of nsp7+8 complexes.

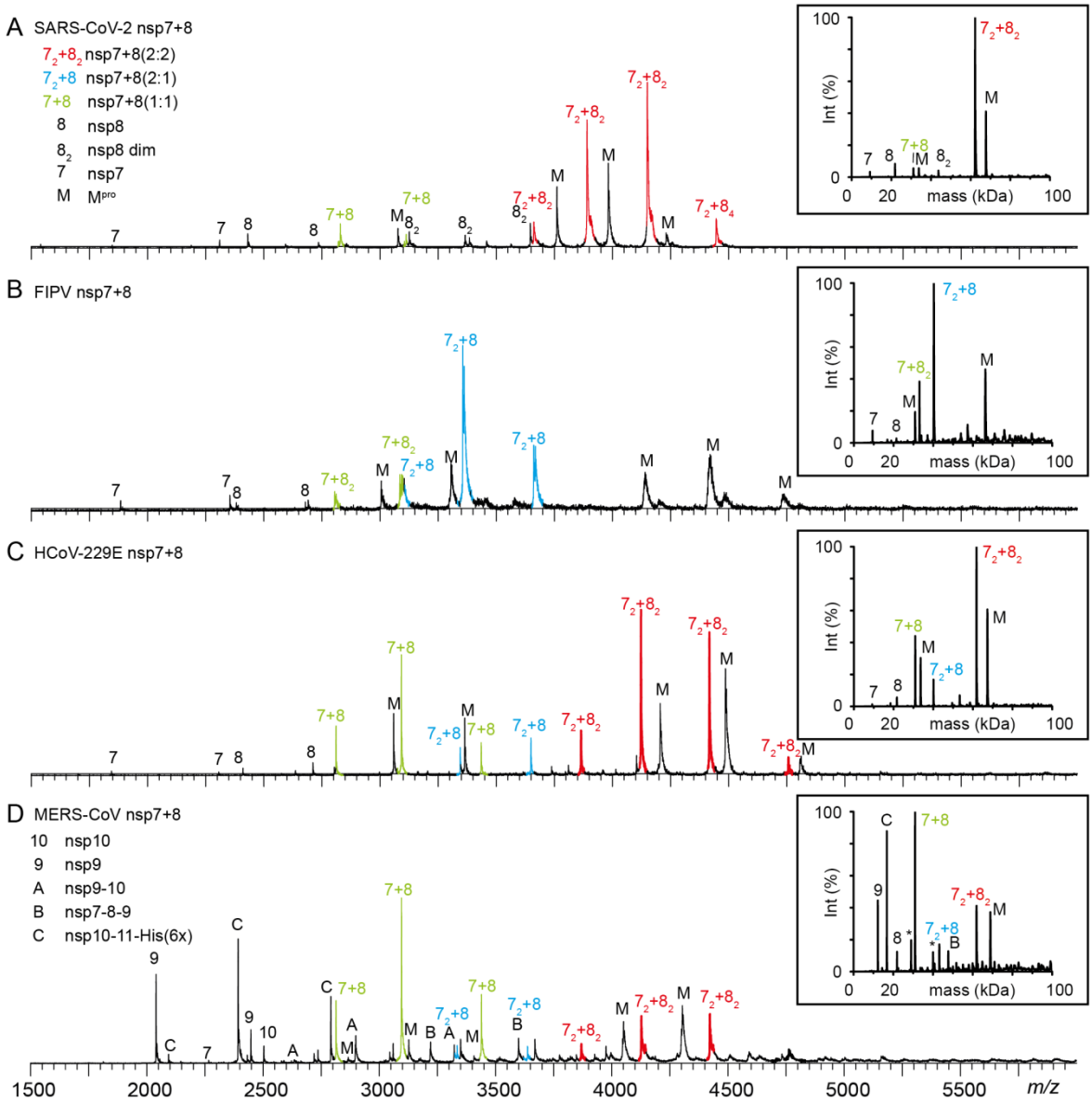

Figure 1: Three complexation groups formed by CoV nsp7+8. Representative mass spectra showing distinct nsp7+8 complexation patterns that were classified into the three groups A, B and AB. Complex formation triggered by M^{pro} (M) mediated cleavage of 15 µM CoV nsp7-8-His_6or MERS-CoV nsp7-11-His_6 precursors in 300 mM ammonium acetate (AmAc), 1 mM DTT, pH 8.0. (**A**) SARS-CoV-2 representing group A forms heterotetramers (nsp7+8 (2:2), red), (**B**) FIPV from group B forms heterotrimers (nsp7+8 (2:1), blue) and (**C**) HCoV-229E from group AB forms both complex stoichiometries (2:2 and 2:1). (**D**) In case of MERS-CoV, also group AB, cleavage of the longer nsp7-11-His_6 precursor resulted in additional processing intermediates (labeled A, B, C). In all three complexation groups, nsp7+8 (1:1) heterodimeric intermediates are observed (green). For spectra of all seven CoV nsp7+8 complexes see Figure S 2.

To ensure authentic nsp7 and nsp8 N- and C-termini, which allow for optimal nsp7+nsp8 complex assembly, the proteins are expressed as nsp7-8-His_6 polyprotein precursors and cleaved by their cognate protease M^{pro} (Figure S 1). Native MS provides an overview of mass

species in solution, while CID-MS/MS confirms the stoichiometry of protein complexes. Distinct oligomerization patterns of nsp7+8 (1:1) heterodimers, (2:1) heterotrimers and (2:2) heterotetramers in the different CoV allowed us to categorize their nsp7+8 complexes into three groups (Figure 1, Figure S 2). SARS-CoV and SARS-CoV-2 (species *Severe acute respiratory syndrome-related coronavirus,* genus *Betacoronavirus*) represent nsp7+8 group A complex formation pattern (Figure 1 A). Consistent with our previous work, SARS-CoV nsp7+8 complexes exist primarily as a heterotetramer comprising two copies of each nsp7 and nsp8 (2:2) [19]. Expectedly, SARS-CoV-2 nsp7+8 form identical (2:2) complexes given the high sequence identity of 97.5 % in the nsp7-8 region (Table S 2). Next, relative peak intensities in native MS of nsp7+8 complexes are converted in a semi-quantitative analysis into abundances of complex species [26]. The heterodimer (2-4 %) is much less abundant than the heterotetramer (96-98 %) suggesting high affinity and hence efficient conversion of heterodimeric intermediates into heterotetramers. Hence, group A only forms two types of nsp7+8 complexes, heterodimers (1:1) and -tetramers (2:2), with the latter clearly being predominant.

In FIPV and TGEV from the species *Alphacoronavirus 1*, genus *Alphacoronavirus*, nsp7 and nsp8 proteins share a sequence identity of 93.9% (Table S 2). Their nsp7+8 complexes are assigned to group B forming predominantly nsp7+8 (2:1) heterotrimers (83 %) and to a lesser extent heterodimers (1:1) (~17 %) (Figure 1 B). An nsp7+8 (2:1) heterotrimeric structure has previously been reported for FIPV but not for TGEV or any other CoV. The association of a single nsp8 with two nsp7 indicates that group B nsp7+8 complexes lack the ability to form tetramers around an nsp8 scaffold.

The third oligomerization pattern is observed for nsp7+8 of HCoV-229E and PEDV, which represent different species in the genus *Alphacoronavirus.* They share only 70.9 % sequence identity in the nsp7-8 region and even less (42-62 %) with the other CoV species examined (Table S 2). PEDV and HCoV-229E nsp7+8 form three major types of oligomers with slightly different efficiencies: heterodimers (1:1), heterotrimers (2:1) and heterotetramers (2:2) (HCoV-229E: 20 %, 12 % and 69 %; PEDV: 52 %, 6 % and 42 %, respectively) (Figure 1 C). By forming both, heterotrimers and -tetramers, these complexes combine properties described above for groups A and B, and are hence categorized into a separate group named accordingly AB. This begs the question whether assembly pathways and structures of heterotetramers in group A and AB are similar. Either, two heterodimers form a

133 heterotetramer around an nsp8 scaffold as in group A [19] or alternatively the heterotrimer
134 recruits another nsp8 subunit to the complex, thus employing an nsp7 core [21]. The latter
135 pathway has recently been reported for SARS-CoV-2 nsp7+8 heterotetramers containing *N*-
136 terminally truncated nsp8 [23].

137 Additionally, nsp7+8 complexation after M^{pro} mediated cleavage of a MERS-CoV nsp7-11-
138 His_6 precursor is compared (Figure 1 D). This larger precursor, comprising nsp7, nsp8, nsp9
139 nsp10 and nsp11, behaves similar to nsp7-9-His_6 (Figure S1) and is used because initial
140 attempts to cleave nsp7-8 only constructs failed. Proteolytic processing of this polyprotein
141 precursor leads to cleavage intermediates (Figure 1 D). Such processing intermediates have
142 been proposed to occur intracellularly and to function distinctly from the individual nsps in
143 e.g. regulation of RTC assembly and viral RNA synthesis [27]. Here, signal intensities of
144 these intermediates provide insights into the processing sequence. Surprisingly, the
145 dominant intermediate is nsp10-11-His_6, despite the small size of nsp11 and a hence expected
146 high accessibility of the nsp10/11 cleavage site. Therefore, slow cleavage and prolonged
147 presence of an nsp10-11 intermediate may have functional implications warranting further
148 studies. Notably, in many CoV polyproteins the nsp10/11 and/or nsp10/12 cleavage sites
149 contain replacements (Pro in MERS-CoV) of the canonical P2 Leu residue conserved
150 throughout most M^{pro} cleavage sites, suggesting that slow or incomplete cleavage is
151 beneficial for these particular sites. Moreover, this cleavage site has different *C*-terminal
152 contexts in the two CoV replicase polyproteins, nsp10-11 in pp1a and nsp10-12 in pp1ab.
153 While the structure of the small nsp11 (~1.5 kDa) is unknown, nsp12 is a large folded protein
154 (~105 kDa), which potentially improves the accessibility of the nsp10/12 site for M^{pro}. Similar
155 effects have been observed for the nsp8/9 cleavage site, which is efficiently cleaved in the
156 protein but not in peptide substrates [19, 28]. The question remains if unprocessed nsp10-11
157 and/or nsp10-12 intermediates exist in virus-infected cells for prolonged times to fulfill
158 specific functions. Other detected intermediates are nsp7-8-9 and nsp9-10 lacking nsp11-His_6.
159 Particularly, the nsp9-10 intermediate has not been identified in our analysis of SARS-CoV
160 nsp7-10 processing, suggesting differences in the *in vitro* processing order between SARS-
161 CoV and MERS-CoV.

162 MERS-CoV nsp7+8 forms heterodimers (1:1), -trimers (2:1) and -tetramers (2:2) (73 %, 8 %
163 and 19 %, respectively), thus demonstrating a group AB complexation pattern. However, we
164 cannot confirm the heterotrimer (2:1) formation by CID-MS/MS due to spectral complexity.

165 Moreover, because of incomplete cleavage as is evident from the cleavage intermediates,
166 signals assigned to the nsp7+8 heterodimer likely overlap with signals of unprocessed nsp7-
167 8. Thus, complete cleavage of nsp7-8 could shift the peak fractions from heterodimer to
168 heterotrimer or -tetramer.

169 **Homodimerization of subunits and precursors.**

170 In the mass spectra of nsp7+8 complexes, monomers and homodimers of nsp7 and nsp8 are
171 also observed. While nsp7 homodimers are identified for all seven CoV species tested, nsp8
172 homodimers are only detected for SARS-CoV and SARS-CoV-2, which belong to group B
173 forming exclusively nsp7+8 heterotetramers around a dimeric nsp8 scaffold (Figure S 3).
174 Moreover, the oligomeric states of the different uncleaved nsp7-8 precursors are probed.
175 Notably, precursors from group B CoVs are mostly monomeric, whereas precursors from
176 group AB and A CoVs are in varying equilibria between monomers and dimers (Figure S 4).
177 The different oligomerization propensities of precursors suggest that molecular interactions
178 driving dimerization of nsp7-8 precursors could critically affect subsequent nsp7+8
179 oligomerization. For SARS-CoV and SARS-CoV-2, the nsp7-8 dimer affinity is low as two-
180 fold dilution to 9 μM shifted the equilibrium towards a monomeric state (Figure S 5). This is
181 in line with our previous findings [19], in which *C*-terminally extended SARS-CoV nsp7-9-
182 His_6 and His_6-nsp7-10 polyprotein constructs were mainly monomeric, suggesting that the
183 presence of the extra *C*-terminal sequence further destabilizes an already weak dimerization.

Collision-induced dissociation reveals complex topology

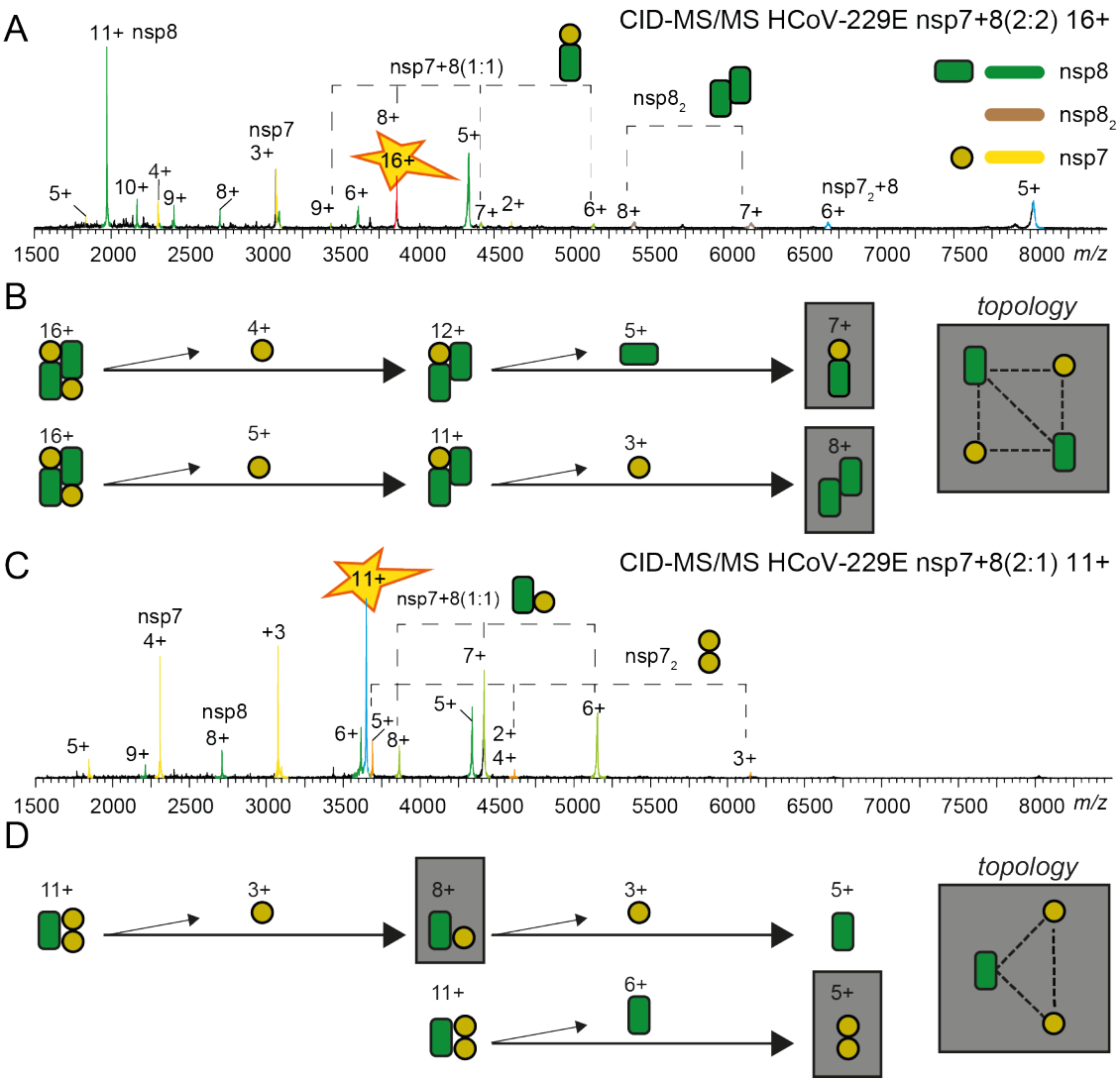

Figure 2: Gas-phase dissociation reveals complex topology. CID-MS/MS product ion spectra (**A** and **C**), dissociation pathways and topology maps (**B** and **D**) for HCoV-229E nsp7+8 (2:1) heterotrimers and (2:2) heterotetramers are shown. With increasing collisional voltage protein complexes are successively stripped from their subunits revealing alternative dissociation pathways. The remaining dimeric species expose direct subunit interactions in the nsp7+8 complexes (grey boxes). Charge states are labeled. (**A** and **B**) The heterotetramers (2:2) undergo two consecutive losses resulting in dimeric product ions of nsp7+8 (1:1) and nsp8$_2$. These products indicate that nsp7:nsp8 and nsp8:nsp8 have direct interfaces in heterotetramers. (**C** and **D**) HCoV-229E heterotrimers dissociate into the dimeric products nsp7+8 (1:1) and nsp7$_2$ indicating direct interfaces between nsp7:nsp8 and nsp7:nsp7 in heterotrimers. All CoV heterotrimers follow similar dissociation pathways, also all CoV heterotetramers follow a common dissociation route, which allow a topological reconstruction of two distinct complex architectures (Figure S 6-Figure S 10).

To deduce the complex topology in the different groups of nsp7+8 interaction patterns, we applied CID-MS/MS using successive subunit dissociations to dissect conserved interactions. CID-MS/MS of the HCoV-229E nsp7+8 heterotetramer (2:2) reveals two dissociation pathways, in which first one nsp7 subunit is ejected from the complex followed by another nsp7 or an nsp8 subunit. After two consecutive losses, the product ions are nsp7+8 (1:1) and

202 $nsp8_2$ dimers, providing evidence for specific subunit interfaces in the complex (Figure 2 A).
203 From these results, the complex topology is deduced as a heterotetramer based on an $nsp8_2$
204 dimer scaffold, in which each nsp8 binds only one nsp7 subunit. Strikingly, this is identical
205 to our previously reported SARS-CoV nsp7+8 heterotetramer (2:2) architecture [19]. In fact,
206 all nsp7+8 (2:2) heterotetramers of groups A and AB (SARS-CoV-2, SARS-CoV, PEDV,
207 HCoV-229E and MERS-CoV) resulted in similar dissociation pathways, subunit interfaces
208 and topology maps, suggesting that these structures are similar across these diverse CoVs.

209 Next, the dissociation pathway of the HCoV-229E nsp7+8 (2:1) heterotrimers is monitored in
210 CID-MS/MS (Figure 2 B). After ejection of one nsp7 or nsp8 subunit, product dimers of
211 nsp7+8 (1:1) and $nsp7_2$ are detected, indicating specific subunit interfaces between nsp7:nsp8
212 and nsp7:nsp7. Again, similar dissociation pathways and subunit interfaces are found for
213 group B and AB heterotrimers (FIPV, TGEV, HCoV-229E and PEDV). Topological
214 reconstructions reveal a heterotrimer forming a tripartite interaction between one nsp8 and
215 two nsp7 subunits. These results agree with the reported X-ray structure of FIPV nsp7+8 [21]
216 and indicate that heterotrimers of these CoVs species have similar arrangements. In turn, this
217 implies that heterotrimers and heterotetramers follow distinct assembly paths.

218 **Chemical cross-linking confirms the formation of specific complexes.**

219 To further support the native MS results, which relies on spraying from volatile salt solutions
220 (e.g. ammonium acetate, AmAc), complementary methods compatible with conventional
221 buffers supplemented with sodium chloride are applied. To provide additional evidence for
222 specific nsp7+8 complex formation, the FIPV and HCoV-229E nsp7+8 complexes are
223 stabilized via crosslinking with glutaraldehyde and subjected to XL-MALDI MS (Cross-
224 linking Matrix-assisted laser ionization MS) (Figure S 11). Peak areas in the MALDI mass
225 spectra are assigned to FIPV nsp7+8 heterodimer, heterotrimer and –tetramer (8.5 %, 9.5 %
226 and 4.2 %, respectively), and HCoV-229E nsp7+8 heterodimer, heterotrimer and –tetramer
227 (6.7 %, 5.3 % and 6.0 %, respectively). The results suggest a higher abundance of nsp7+8
228 heterodimer and -trimer complexes in FIPV than in HCoV-229E, while HCoV-229E contains
229 more heterotetramers. This largely agrees with the results from native MS. However, the
230 MALDI mass spectra show high background of virtually all possible nsp7+8 stoichiometries
231 (<200,000 m/z), probably due to over-crosslinking with the rather unspecific glutaraldehyde.

To refine these results, nsp7+8 complexes are stabilized with the amine specific crosslinker BS^3 and analyzed by SDS-PAGE (Figure S 12). Multiple stoichiometries are identified with a few prominent bands highlighting the main complexes generated. These bands are assigned to SARS-CoV nsp7+8 heterodimers and -tetramers, FIPV nsp7+8 heterodimers and -trimers and HCoV-22E nsp7+8 heterodimers, heterotrimers and -tetramers of HCoV-229E, providing additional support for the classification of nsp7+8 complexes into groups A (SARS-CoV), B (FIPV) and AB (HCoV-229E).

Light scattering provides insights into complexation at high protein concentrations

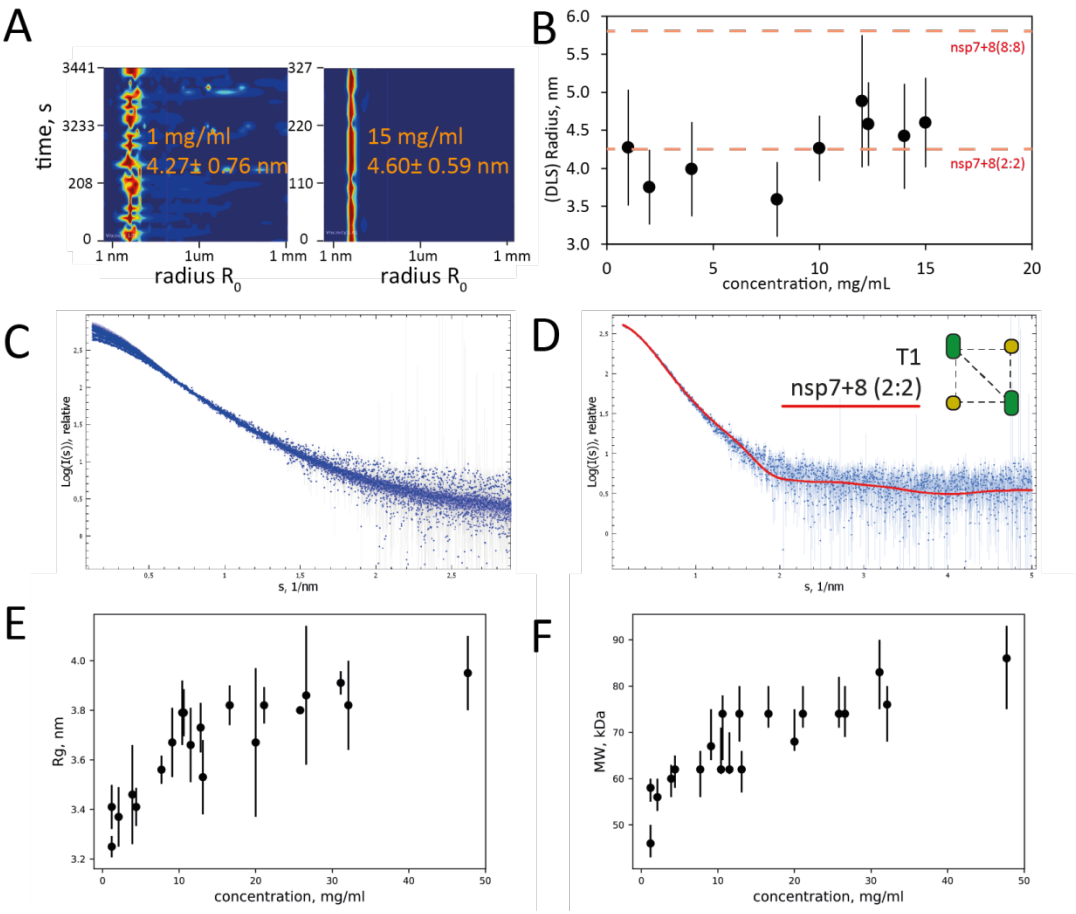

Figure 3: DLS and SAXS reveal oligomeric state of SARS-CoV-2 nsp7+8 at higher protein concentrations. At increasing protein concentrations, the hydrodynamic radius (R_0) remains stable but becomes more homogenous in DLS. (**A**) shows two exemplary DLS plots (1 mg/ml; 15 mg/ml) and (**B**) how the radius R_0 develops with increasing protein concentration. Theoretical hydrodynamic radii ($R_{0,theo}$) of heterotetramer and hexadecamer candidate structures are indicated (red dashed lines). (**C**) displays SAXS curves collected at different solute concentrations and (**D**) the fit of the curve computed from T1 tetramer (red line) to the SAXS data collected at 1.2 mg/mL (blue dots with error bars). (**E**) Radius of gyration (R_g) and (**F**) molecular weight estimated from the SAXS data both stabilize with increasing concentration like in DLS on values that are in agreement with the $R_{0,theo}$ of the T1 nsp7+8 (2:2) heterotetramer.

251 To test the stoichiometry at higher protein concentrations in solution, dynamic light
252 scattering (DLS) of SARS-CoV-2 nsp7+8 from 1 to 15 mg/mL is performed (Figure 4 A). No
253 significant increase of the hydrodynamic radius (R_0) occurrs with increasing concentration.
254 At the same time, the measured radii become more stable and fluctuate less, which suggests
255 a shift towards higher complex homogeneity and a reduced fraction of free nsp7 and nsp8.

256 For SARS-CoV-2, no complex structure is available for full-length nsp7+8 proteins but,
257 previously, a SARS-CoV nsp7+8 (8:8) has been reported using X-ray crystallography [20],
258 where high protein concentrations are deployed. In order to relate the average experimental
259 hydrodynamic radius ($R_{0,exp}$ = 4.25 ± 0.61 nm) to candidate structures, the theoretical
260 hydrodynamic radius is calculated for the SARS-CoV nsp7+8 (8:8) hexadecamer
261 ($R_{0,theo}$ = 5.80 ± 0.29 nm) and a subcomplex thereof, a putative nsp7+8 heterotetramer (2:2) in
262 T1 conformation ($R_{0,theo}$ = 4.52 ± 0.27 nm) (Figure S 13). This is the only model with full-length
263 nsp8 that agrees with the stoichiometry and topology determined by native MS. At
264 physiologically relevant concentrations from 1 to 10 mg/mL, the average experimental
265 hydrodynamic radius agrees well with the theoretical hydrodynamic radius of the
266 heterotetramer T1. Hence a heterotetramer is likely the prevailing species in solution (Figure
267 4 B).

268 To underpin the DLS results, SAXS data are collected on solutions of nsp7+8 at
269 concentrations ranging from 1.2 to 47.7 mg/ml. The normalized SAXS intensities increase at
270 low angles with increasing concentration (Figure 4 B and Table S 3), suggesting a change in
271 the oligomeric equilibrium and a formation of larger oligomers. This trend is well illustrated
272 by the evolution of the apparent radius of gyration and molecular weight of the solute
273 determined from the SAXS data (Figure 4 E and F). The increase in the effective molecular
274 weight, from about 50 to 80 kDa suggests that the change in oligomeric state is limited and
275 that the tetrameric state (MW_{theo}: 62 kDa) remains predominant in solution.

276 The SAXS data at low concentrations (<4 mg/mL) fit well the computed scattering from
277 heterotetramer T1 but misfits appear at higher concentration (Figure 4 D, structure of T1
278 shown in Figure S 13and the discrepancy χ^2 reported in Table S 4). Mixtures of
279 heterotetramers and hexadecamers cannot successfully fitted to the higher concentration
280 data either (Figure S 14). To further explore the oligomeric states of nsp7+8, a dimer of T1 is
281 used to simultaneously fit the curves collected at different concentrations by a mixture of

282 heterotetramers and -octamers. Reasonable fits to all SAXS data are obtained with volume
283 fractions of heterooctamers growing from 0 to 0.52 with increasing concentration (Figure S
284 14). Based on the flexibility of the molecule and the multiple possible binding sites between
285 nsp7 and nsp8, it is not surprising that larger assemblies are observed at very high solute
286 concentrations. The SAXS and DLS results provide evidence that the nsp7+8 (2:2)
287 heterotetramer is the prevailing stoichiometry in solution at physiological concentrations (1-
288 10 mg/mL with volume fractions between 1 and 0.7).

289 **Potential implications of sequence conservation on heterotrimer and -tetramer**
290 **formation.**

291 To extend this analysis, we select candidate structures in agreement with the stoichiometry
292 and topology observed (Figure S 10). For the heterotetramer, two conformers of nsp7+8 (2:2)
293 subcomplexes, T1 and T2, of correct architecture can be extracted from the larger SARS-CoV
294 nsp7+8 hexadecamer [20] (pdb 2ahm), (Figure S 13 A). Both conformers constitute a head to
295 tail interaction of two nsp7+8 heterodimers mediated by an nsp8-nsp8 interface. Notably,
296 nsp8 in T1 is more extended, revealing an almost full-length amino acid sequence (2-193),
297 while in T2 the nsp8 *N*-terminal 35 to 55 residues are unresolved. For the heterotrimeric
298 complexes, the only deposited structure is the FIPV nsp7+8 (2:1) heterotrimer [21] (pdb
299 3ub0), which agrees well with our experimental topology (Figure S 13 B).

300 In order to identify molecular determinants for heterotrimer or -tetramer formation, the
301 candidate structures are examined for molecular contacts (van der Waals radius -0.4 Å). The
302 conservation of contact residues is evaluated in a sequence alignment to identify possible
303 determinants of different stoichiometries (Figure S 15). Notably, most amino acids lining
304 subunit interfaces in heterodimers, -trimers and -tetramers are conserved. The interfaces in
305 the candidate structures occupy two common structural portions of the nsp8 subunit (Figure
306 4 A). The first binding site (BS I) is located between the nsp8 head and shaft domain,
307 responsible for binding of nsp7 (I) in heterodimer formation, as seen in all available high
308 resolution structures of nsp7+8 [20-23] and the polymerase complex [13-16]. The second
309 binding site (BS II) appears highly variable in terms of its binding partner and lies at the nsp8
310 elongated *N*-terminus. In fact, one largely conserved motif (res60-70) is responsible for the
311 main contacts in the entire candidate complexes selected based on our data: nsp7+8 (2:2) T1
312 and T2 for the heterotetramer and nsp7+8 (2:1) for the heterotrimer. The respective
313 sidechains take positions on one side of the nsp8 α-helix and have the ability to form

interactions with either mainly nsp7 (partly nsp8) in the SARS-CoV nsp7+8 (2:2) heterotetramer T1, mainly nsp8 (partly nsp7) in the SARS-CoV nsp7+8 heterotetramer T2 or only nsp7 in the FIPV nsp7+8 (2:1) heterotrimer (Figure S 16 A-C). Due to its sequence conservation, it is unlikely that alone this motif at BS II has a decisive impact for heterotrimer or -tetramer formation.

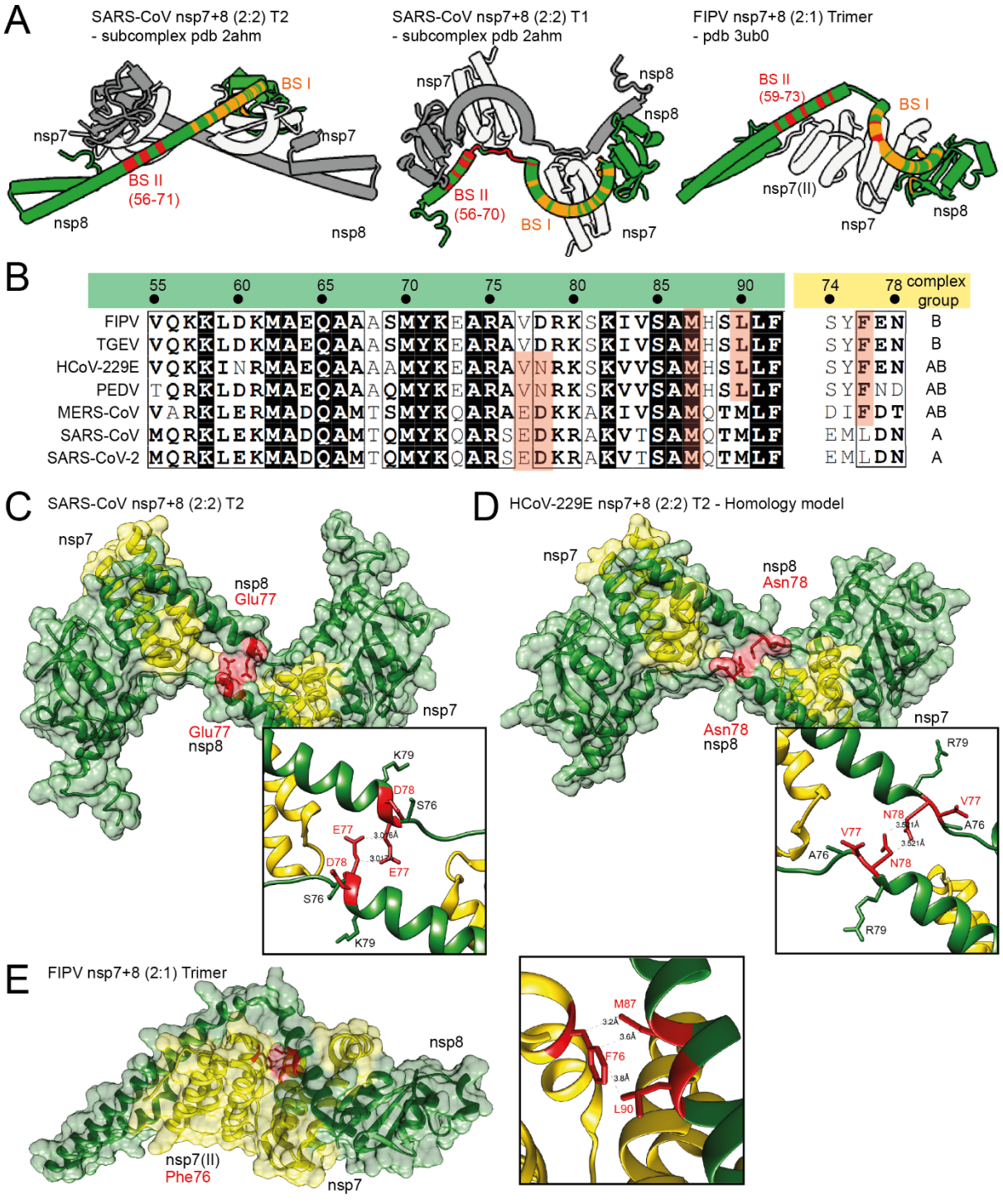

Figure 4: Candidate structures and sequence conservation of nsp7+8 heterotrimers and -tetramers. Candidate structures for nsp7+8 heterotetramer and –trimer are chosen based on experimental stoichiometry and topology

in solution. (**A**) shows two conformers of SARS-CoV nsp7+8 (2:2) heterotetrameric subcomplexes, T1 (left) and T2 (middle), from the larger (8:8) heterohexadecamer (pdb 2ahm) and the FIPV nsp7+8 (2:1) heterotrimer (right, pdb 3ub0). Complexes exhibit two similar binding sites in nsp8, BS I (orange) and BS II (red). For simplification binding sites are only shown for one nsp8 subunit (green). BS II is additionally labelled with nsp8 residue (res) number forming the main interaction patch (BS II contact residues see Figure S 15). (**B**) Sequence alignment of nsp8 (green, res55-92) and nsp7 (yellow, res74-78) is displayed for the seven CoVs. Two heterotrimer or -tetramer specific contact sites (red) exhibit sequence conservation well in line with the complexation groups determined by native MS. (**C**) In SARS-CoV T2, nsp8 Glu77 comes into contact with nsp8 Glu77, a unique heterotetramer interaction, (**D**) which in a homology model of HCoV-229E based on T2 is replaced by nsp8 Asn78. (**E**) The FIPV heterotrimer structure shows nsp7 Phe76, binding to nsp8 Met87 and Leu90, a contact unique for the heterotrimer forming species. Insets show magnification of contact sites. Closest distances (3.0-3.8 Å) for relevant residues in contact (red) are given.

Therefore, unique interactions could exist, which explain the shift in complex stoichiometry from heterotrimer to -tetramer observed in the different CoVs categorized into group A, AB and B (Figure 4 B). Here, we identify a possibly heterotetramer stabilizing contact site in T2, where nsp8 Glu77 self-interacts with nsp8II Glu77, which gives the complex density and compactness (Figure 4 C). This residue is only present in nsp8 of SARS-CoV and SARS-CoV-2 from group A and MERS-CoV of group AB. However, homology models suggest that in the other tetramer forming complexes of group AB, HCoV-229E and PEDV, nsp8 Asn78 could partially replace this interaction (Figure 4 D). This is different in group B viruses, forming only heterotrimers, where residues at these positions are nsp8 Val77 and Asp78, with the Asp78 possibly being solvent exposed and hence unable to replace this interaction. Furthermore, we also identify a contact site possibly stabilizing the heterotrimer in the crystal structure of the FIPV nsp7+8 (2:1), which reveals that a second subunit of nsp7 (nsp7II) is locked via Phe76 to nsp8 (Figure 4 E). Importantly, this residue is uniquely conserved among trimer forming complexes of group B and group AB, but replaced by nsp7 Leu76 in the strictly heterotetramer forming group A.

These findings are compared to the recently released structure of the polymerase complex (pdb 6xez, Figure S 16 D and E), comprising nsp7+8+12+13(1:2:1:2) [29]. The residues potentially responsible for a shift in quaternary structure, nsp8 Glu77 or Asp78 and nsp7 Phe76, are distant from any protein-protein or protein-RNA interaction and thus are not expected to play a role in polymerase complex formation. Surprisingly, the identical set of residues in BS II supports all interactions (Glu60, Met62, Ala63, Met67 and Met70) between nsp8b and nsp12/nsp13.1 and between nsp8a and nsp13b (Figure S 16 D and E). Notably, within the polymerase complex amino acids involved in RNA binding point in the opposite direction of the protein interfaces and have little or no role in nsp7+8 complex formation.

359 **Discussion**

360 Our findings reveal the nsp7+8 quaternary composition of seven CoVs representing five
361 coronavirus species of the genera *Alpha*- and *Betacoronavirus*. Viruses of the same species
362 (SARS-CoV/SARS-CoV-2 and TGEV/FIPV, respectively) produce the same type of nsp7+8
363 complexes. Next to a conserved nsp7+8 heterodimer (1:1), the inherent specificity of nsp7+8
364 complex formation categorizes them into three groups: group A forming only
365 heterotetramers (2:2), group B forming only heterotrimers (2:1) and group AB forming both
366 heterotetramers (2:2) and heterotrimers (2:1). Complexes of the same stoichiometry exhibit a
367 conserved topology, consisting of an nsp8 homodimeric scaffold for the heterotetramers and
368 an nsp7 homodimeric core for the trimers. Candidate structures based on our results
369 highlight *Alpha*- and *Betacoronavirus*-wide conserved binding sites on nsp8, named BS I and
370 BS II, which provide the modular framework for a variety of complexes. Furthermore,
371 unique molecular contacts for the complex groups have the potential to determine the ability
372 and preference for heterotrimer and/or heterotetramer formation.

373 We provide evidence that, even at high concentrations, the SARS-CoV-2 nsp7+8
374 heterotetramer (2:2) represents the predominant species. In order to relate our results to *in*
375 *vivo* conditions, we consider the following aspects: According to maximum molecular
376 crowding [30], polyproteins pp1a and pp1ab can reach a maximum of 125-450 μM, which
377 translates to 3.9-11.7 mg/mL nsp7+8. This range is covered by our DLS and SAXS analysis. In
378 absence of other interaction partners, we expect that, *in vivo*, the nsp7+8 (2:2) heterotetramer
379 represents the predominant nsp7+8 complex of SARS-CoV-2 and other heterotetramer
380 forming CoVs of complexation groups A and AB.

381 The heterotetramer candidate structures and models presented here are based on the
382 conformers T1 or T2 of the SARS-CoV heterohexadecamer structure, which contains full-
383 length nsp8 [20]. Although, our results cannot clarify, if one of these conformers is the
384 biologically relevant structure existing in solution, the combined evidence provided here
385 strongly suggests structural similarity to T1/T2. Considering the crystallographic origin of
386 T1/T2 and the overlap of binding sites, the heterotetramer could well be a flexible and
387 dynamic structure in solution.

388 In contrast to our findings, a SARS-CoV nsp7+8 hexadecamer structure has been reported
389 [20]. However, this structure has been derived from X-ray crystallography, hence showing a

390 static, frozen state, where the crystal lattice formation favors stabilized arrangements that
391 could differ from the solution state of the protein complexes. In the case of nsp8, the flexible
392 *N*-terminus could inhibit crystal formation, and has been removed in some studies [22, 23].
393 Alternatively, it may stabilize specific interactions, thereby promoting crystal formation by
394 binding to one of the multiple interfaces presented between nsp7 and nsp8, resulting in a
395 physiologically irrelevant larger oligomeric structure. The SAXS data presented here
396 partially supports this scenario at high protein concentrations but also confirms a
397 predominantly heterotetrameric assembly in solution. Thus, a potential shift of quaternary
398 structure from heterotetramer towards a higher-order complex, such as a heterohexadecamer
399 appears unlikely unless triggered e.g. by binding to nucleic acids as has been repeatedly
400 described for nsp7+8 complexes [20].

401 All seven CoV nsp7 and nsp8 proteins shown here also form heterodimers (1:1). Such
402 heterodimeric subcomplexes with nsp7 bound to nsp8 BS I have been observed in all
403 deposited complex structures containing nsp7+8 [20-23] or nsp12 [13-16]. Therefore, the
404 heterodimer represents the most basic form of nsp7+8 complexes and likely serves as
405 universal substructure building block in the coordinated assembly of functional RTCs of
406 CoVs from the genera *Alpha-* and *Betacoronavirus*. Moreover, heterotrimer and -tetramer
407 formation are based on a second canonical binding site at the nsp8 *N*-terminal domain, BS II.
408 This site appears to have a high propensity to form complexes with various binding partners
409 (e.g. nsp7+8, nsp12 or nsp13). Accordingly, our analysis suggests that the nsp8 BS II strives
410 for occupation. The nsp7+8 quaternary composition, topology and analysis of binding sites
411 presented here allow us to reconstruct and propose a model of the complex formation
412 pathway (Figure 5).

413 The preference for heterotrimer and -tetramer can probably be pinpointed to just a few
414 amino acids within nsp8 BS II or interacting with it. Here, we identify two contacts that
415 could have unique discriminatory potential for promoting heterotrimeric (nsp7 Phe76) or
416 heterotetrameric (nsp8 Glu77 and Asn78) quaternary structures. Notably in presence of nsp7
417 Phe76 and nsp8 Asn78, as observed for group AB, the heterotetramer is always more
418 abundant than the heterotrimer. However, compared to the entire BS II, theses contacts only
419 represent a small share of the binding interface and contribute little interaction energy
420 through van der Waals forces. Nevertheless, the unique position of their contacts could
421 critically determine the types of interactions with one or another binding partner.

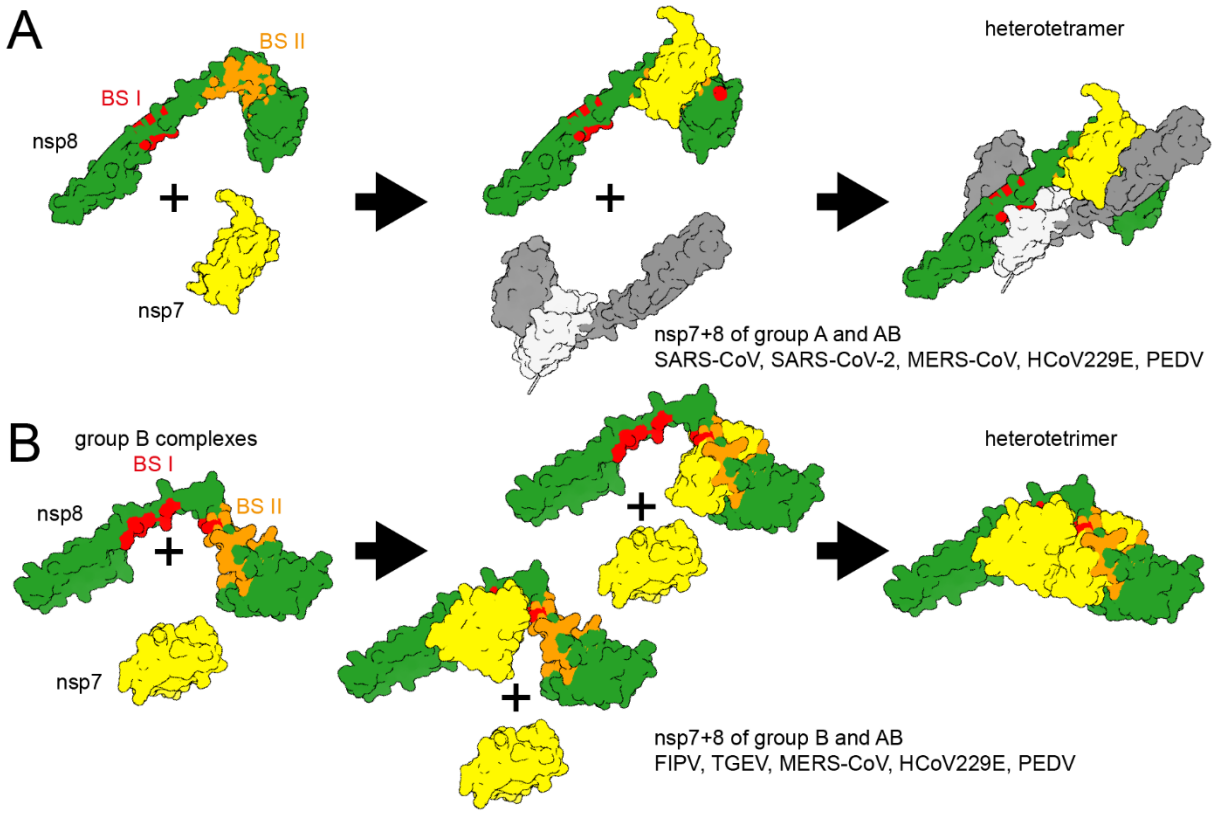

Figure 5: Proposed model for nsp7+8 complex formation. (**A**) For complexes of group A, heterodimers form via nsp8 BS I, which quickly dimerize via BS II into a heterotetramer. A theoretic route via a preformed nsp8 scaffold is unlikely to play a role in heterotetramer formation since no nsp7+8 (1:2) intermediates are observed for complexes of SARS-CoV or SARS-CoV-2. Moreover,, nsp7 and nsp8 occupy neighboring positions in the replicase polyproteins, thus favoring their interaction (*in cis*) at early stages in the infection cycle (when intracellular viral polyprotein concentrations are low) over intermolecular interactions between different replicase polyprotein molecules as is also evident from the low dimerization ability of the precursors. (**B**) For group B complexes, we propose the formation of a heterodimer intermediate via nsp8 BS I or BS II and subsequent recruitment of a second nsp7, resulting an nsp7+8 (2:1) heterotrimer. This is also supported by the relatively high peak fractions of heterodimers detected. Group AB complexes can use both complexation pathways. In line with this, the proteins also produce a relatively high heterodimer signal but, ultimately, prefer to form heterotetramers rather than heterotrimers.

Since the critical residues required for nsp7+8 complex formation have no overlap with nsp12 interaction sites, direct docking of preformed heterotrimers and -tetramers to nsp12 can be expected. Furthermore, heterotrimeric and -tetrameric structures are compatible with accommodation of specific RNA structures similar to what has been suggested for heterohexadecameric nsp7+8 by Rao et al. [14]. Notably, if heterotrimeric or -tetrameric nsp7+8 structures were associated with nsp12, the binding site for nsp13 would be blocked, which may have regulatory implications for CoV replication. Altogether, these conserved binding mechanisms and overlapping binding sites confirm the proposed role of nsp8 as a major interaction hub within the CoV RTC [31], and indicate critical regulatory functions by specific nsp7+8 complexes.

445 Finally, we can only speculate about possible reasons for the existence of different nsp7+8
446 complexes: (1) Similar kinetic stability due to occupation of both binding sites (both
447 structures exist because they are equally efficient in occupying BS I and BS II), (2) unknown
448 functional relevance in CoV replication (e.g. specificity to RNA structures channeled to the
449 nsp12 RdRp) or (3) adaption to host factors and possible regulatory functions.

450 In summary, our work shows, and provides a framework to understand, the characteristic
451 distribution and structures of nsp7+8 (1:1) heterodimer, (2:1) heterotrimers and (2:2)
452 heterotetramers in representative alpha- and betacoronaviruses. The nsp7+8 structure in
453 solution can be used to investigate its independent functional role in the formation of active
454 polymerase complexes and, possibly, regulation and coordination of polymerase and other
455 RTC activities, for example in the context of antiviral drug development targeting different
456 subunits of CoV polymerase complexes reconstituted *in vitro*.

457 **Material and Methods**

458 **Cloning and gene constructs**

459 The codon optimized sequence for the SARS-CoV-2 nsp7-8 region (NC_045512.2) was
460 synthesized by Eurofins scientific SE with overhangs suitable for insertion into pASK-
461 IBA33plus plasmid DNA (IBA Life Sciences). A golden gate assembly approach using Eco31I
462 (BsaI) (Thermo Fisher Scientific) was used to shuttle the gene into the plasmid. Linker and
463 tag of the expression construct SARS-CoV-2 nsp7-8-His_6 contained the *C*-terminal amino
464 acids –SGSGSARGS-His_6 (SGSG residues as P1′-P4′ of Mpro cleavage site and SARGS-His_6
465 residues as the default linker of pASK vectors). The SARS-CoV nsp7-8 pASK33+ plasmid
466 generated previously [21, 32] was used for the expression of SARS-CoV nsp7-8-His_6
467 containing the *C*-terminal amino acids –SARGS-His_6. The expression plasmid for SARS-CoV
468 M^{pro} was generated as described by Xue et al.[33]. To produce nsp7-8-SGSGSARGS-His_6
469 precursor proteins in *Escherichia coli*, the nsp7-8 coding sequences of HCoV-229E (HCoV-
470 229E; GenBank accession number AF304460), FIPV (FIPV, strain 79/1146; DQ010921), SARS-
471 CoV (strain Frankfurt-1; AY291315), PEDV (PEDV, strain CV777, NC_003436) and TGEV
472 (TGEV, strain Purdue; NC_038861) were amplified by reverse transcription-polymerase
473 chain reaction (RT-PCR) from viral RNA isolated from cells infected with the respective
474 viruses and inserted into pASK3-Ub-CHis_6 using restriction- and ligation-free cloning
475 methods as described before (Tvarogová et al., 2019). Similarly, the nsp7-9 or nsp7-11 coding

476 region of MERS-CoV (strain HCoV-EMC; NC_019843), was amplified by RT-PCR from
477 infected cells and inserted into pASK3-Ub-CHis$_6$. The HCoV-229E and FIPV nsp5 coding
478 sequences were cloned into pMAL-c2 plasmid DNA (New England Biolabs) for expression
479 as MBP fusion proteins containing a *C*-terminal His$_6$-tag. Primers used for cloning and
480 mutagenesis are available upon request.

481 **Expression and purification**

482 SARS-CoV M^{pro} was produced with authentic ends as described in earlier work [33]. To
483 produce the precursors, SARS-CoV and SARS-CoV-2 nsp7-8-His$_6$, BL21 Rosetta2 (Merck
484 Millipore) were transformed, grown in culture flasks to OD_{600} = 0.4-0.6, then induced with
485 50 µM anhydrotetracycline and continued to grow at 20 °C for 16 h. For pelleting, cultures
486 were centrifuged (6000 × *g* for 20 min) and cells were frozen at -20 °C. Cell pellets were lysed
487 in 1:5 (*v*/*v*) buffer B1 (40 mM phosphate buffer, 300 mM NaCl, pH 8.0) with one freeze-thaw
488 cycle, sonicated (micro tip, 70 % power, 6 times on 10 s, off 60 s; Branson digital sonifier SFX
489 150) and then centrifuged (20,000 × *g* for 45 min). Proteins were isolated with Ni^{2+}-NTA beads
490 (Thermo Fisher Scientific) in gravity flow columns (BioRad). Proteins were bound to beads
491 equilibrated with 20 column volumes (CV) B1 + 20 mM imidazole, then washed with 20 CV
492 B1 + 20 mM imidazole followed by 10 CV of B1 + 50 mM imidazole. The proteins were eluted
493 in eight fractions of 0.5 CV B1 + 300 mM imidazole. Immediately after elution, fractions were
494 supplemented with 4 mM DTT. Before analysis with native MS, Ni^{2+}-NTA eluted fractions
495 containing the polyprotein were concentrated to 10 mg/mL and further purified over a
496 10/300 Superdex 200 column (GE healthcare) in 20 mM phosphate buffer, 150 mM NaCl,
497 4 mM DTT, pH 8.0. The main elution peaks contained nsp7-8. For quality analysis, SDS-
498 PAGE was performed to assess the sample purity.

499 To obtain a pre-purified SARS-CoV-2 nsp7+8 complex for DLS and SAXS, eluate fractions
500 from the Ni^{2+}-NTA column containing the nsp7-8-His$_6$ were concentrated and the buffer
501 exchanged with a PD-10 desalting column (GE Healthcare) equilibrated with 50 mM Tris,
502 pH 8.0, 100 mM NaCl, 4 mM DTT and 4 mM $MgCl_2$ (SEC-buffer). Then nsp7-8-His$_6$ was
503 eluted with 3.5 mL SEC-buffer and subsequently cleaved with M^{Pro}-His$_6$ (1:5, M^{Pro}-His$_6$: nsp7-
504 8-His$_6$) for 16 h at RT. M^{pro}-His$_6$ was removed with Ni-NTA agarose and the cleaved nsp7+8
505 complex was subjected to a HiLoad 16/600 Superdex 75 pg size exclusion column
506 equilibrated with SEC-buffer.

507 The HCoV-229E, PEDV, FIPV and TGEV nsp7-8-His_6 and MERS-CoV nsp7-11-His_6 precursor
508 proteins were produced and purified as described before (Tvarogová et al., 2019) with a
509 slightly modified storage buffer. Anion exchange chromatography fractions of the peak
510 containing the desired protein were identified by SDS-PAGE, pooled and dialyzed against
511 storage buffer (50 mM Tris-Cl, pH 8.0, 200 mM NaCl and 2 mM DTT).

512 MBP-nsp5-His_6 fusion proteins were purified using Ni^{2+}-IMAC as described before
513 (Tvarogová et al., 2019). To produce HCoV-229E and FIPV MBP-nsp5-His_6, *E. coli* TB1 cells
514 were transformed with the appropriate pMAL-c2-MBP-nsp5-His_6 construct and grown at
515 37 °C in LB medium containing ampicillin (100 µg/mL). When an OD_{600} of 0.6 was reached,
516 protein production was induced with 0.3 mM isopropyl β-D-thiogalactopyranoside (IPTG)
517 and cells were grown for another 16 h at 18 °C. Thereafter, the cultures were centrifuged
518 (6000 × *g* for 20 min) and the cell pellet was suspended in lysis buffer (20 mM Tris-Cl, pH 8.0,
519 300 mM NaCl, 5 % Glycerol, 0.05 % Tween-20, 10 mM imidazole and 10 mM β-
520 mercaptoethanol) and further incubated with lysozyme at 4 °C (0.1 mg/mL) for 30 min.
521 Subsequently, cells were lysed by sonication and cell debris was removed by centrifugation
522 for 30 min at 40,000 × *g* and 4°C. The cell-free extract was bound to pre-equilibrated Ni^{2+}-NTA
523 (Qiagen) matrix for 3 h. Ni^{2+}-IMAC elution fractions were dialyzed against buffer comprised
524 of 20 mM Tris-Cl, pH 7.4, 200 mM NaCl, 5 mM $CaCl_2$ and 2 mM DTT and cleaved with
525 factor Xa to release nsp5-His_6. Then, nsp5-His_6 was passed through an amylose column and
526 subsequently bound to Ni^{2+}-NTA matrix to remove any remaining MBP. Following elution
527 from the Ni^{2+}-NTA column, nsp5-His_6 was dialyzed against storage buffer (20 mM Tris-Cl,
528 pH 7.4, 200 mM NaCl and 2 mM DTT) and stored at -80 °C until further use.

529 **Native mass spectrometry**

530 To prepare samples for native MS measurements, M^{pro} was buffer exchanged into 300 mM
531 AmAc, 1 mM DTT, pH 8.0 by two cycles of centrifugal gel filtration (Biospin mini columns,
532 6,000 MWCO, BioRad) and the precursors were transferred into 300 mM AmAc, 1 mM DTT,
533 pH 8.0 by five rounds of dilution and concentration in centrifugal filter units (Amicon,
534 10,000 MWCO, Merck Millipore). Cleavage and complex formation was started by mixing
535 nsp7-8-His_6 and protease M^{pro} with final concentrations of 15 µM and 3 µM, respectively.
536 Three independent reactions were started in parallel and incubated at 4 °C overnight.

537 Tips for nano-electrospray ionization (nanoESI) were pulled in-house from borosilicate
538 capillaries (1.2 mm outer diameter, 0.68 mm inner diameter, with filament, World Precision
539 Instruments) with a micropipette puller (P-1000, Sutter Instruments) using a squared box
540 filament (2.5 × 2.5 mm, Sutter Instruments) in a two-step program. Subsequently, tips were
541 gold-coated using a sputter coater (Q150R, Quorum Technologies) with 40 mA, 200 s, tooling
542 factor 2.3 and end bleed vacuum of 8×10^{-2} mbar argon.

543 Native MS was performed at a nanoESI quadrupole time-of-flight (Q-TOF) instrument (Q-
544 TOF2, Micromass/Waters, MS Vision) modified for higher masses [34]. Samples were ionized
545 in positive ion mode with voltages applied at the capillary of 1300-1500 V and at the cone of
546 130-135 V. The pressure in the source region was kept at 10 mbar throughout all native MS
547 experiments. For desolvation and dissociation, the pressure in the collision cell was
548 1.5×10^{-2} mbar argon. For native MS, accelerating voltages were 10 - 30 V and quadrupole
549 profile 1,000 - 10,000 *m/z*. For CID-MS/MS, acceleration voltages were 30 - 200 V. Raw data
550 were calibrated with CsI (25 mg/mL) and analyzed using MassLynx 4.1 (Waters). Peak
551 deconvolution and determination of relative intensity was performed using UniDec [35]. All
552 determined masses are provided (Table S 1).

553 **XL-MALDI**

554 Pre-purified FIPV nsp7+8 and HCoV-229E nsp7+8 at 20 µM were cross-linked with 0.15 %
555 glutaraldehyde (Sigma-Aldrich) at 4 °C for 25 min before diluting them to 1 µM in MALDI
556 matrix solution (sinapinic acid 10 mg/mL in acetonitrile/water/TFA, 49.95/49.95/0.1, *v/v/v*)
557 and spotting (1 µL) onto a stainless steel MALDI target plate. The MALDI-TOF/TOF mass
558 spectrometer (ABI 4800, AB Sciex) equipped with a high-mass detector (HM2, CovalX) was
559 used in linear mode. For acquiring mass spectra (1,000 to 1,000,000 *m/z*) spots were ionized
560 with a Nd:YAG laser (355 nm) and 500 shots per spectrum were accumulated. Obtained raw
561 data were smoothed and analyzed using mMass (v5.5.0, by Martin Strohalm [36]).

562 **DLS**

563 To check the monodispersity of the samples and to study the stoichiometry of the nsp7+8
564 complexes, DLS measurements were performed with the Spectro Light 600 (Xtal Concepts).
565 The complex was concentrated to various concentrations and samples were spun down for
566 10 min at 12,000 rpm and 4 °C. A Douglas Vapour batch plate (Douglas instruments) was

filled with paraffin oil and 2 μL of each sample was pipetted under oil. DLS measurements for each sample were performed at 20 °C with 20 measurements for 20 s each, respectively.

SAXS

SAXS data were collected on the P12 beamline of EMBL at the PETRA III storage ring (DESY, Hamburg). X-ray wavelength of 1.24 Å (10 keV) was used for the measurements, scattered photons were collected on a Pilatus 6M detector (Dectris), with a sample to detector distance of 3 m. Data were collected on 22 concentrations ranging from 1.2 to 48 mg/mL nsp7+8 in 50 mM Tris, pH 8.0, 100 mM NaCl, 4 mM DTT and 4 mM $MgCl_2$, pure buffer was measured between samples. For each data collection, 20 frames of 100 ms were collected. 2D scattering images were radially averaged and normalized to the beam intensity. The frames were compared using the program Cormap [37, 38], and only similar frames were averaged and used for further analysis to avoid possible beam-induced effects. Scattering collected on the pure buffer was subtracted from that of the sample and the resulting curves were normalized to the protein concentration to obtain the scattering of nsp7+8 complexes.

The data processing pipeline SASflow was used for data reduction and calculation of the overall SAXS parameters [38]. Molecular weights were inferred from different molecular calculation methods using a Bayesian assessment [39]. The program CRYSOL was used to compute the theoretical curves from the atomic structures [40]. Volume fractions of the components of the oligomeric mixtures were computed and fitted to the data using the program OLIGOMER [41]. The dimer of T1 was built by the program SASREFMX [42], which builds a dimeric model that fits best, in mixture with the monomeric T1, multiple scattering curves collected at different concentrations.

Visualization

Molecular graphics and analyses were performed with UCSF ChimeraX, developed by the Resource for Biocomputing, Visualization, and Informatics at the University of California, San Francisco, with support from National Institutes of Health R01-GM129325 and the Office of Cyber Infrastructure and Computational Biology, National Institute of Allergy and Infectious Diseases.

Acknowledgements

We would like to thank the XBI User consortium for providing the instrumentation and laboratories at the European XFEL.

Author contributions

Conceptualization and methodology - B.K., C.S., C.U. G.B., R.M. and J.Z.; plasmid construction and protein production - B.K., C.S., G.B. , L.B.; providing research materials C.U., K.L. and J.Z.; XL-MALDI-MS - B.K., M.K. and R.Z.; SAXS: C.B., D.S. Investigation - B.K., G.B., C.S., R.S. Discussion of results - B.K., C.S., C.U., K.L., R.M., G.B., J.Z.; Formal analysis and visualization - B.K.; Original Draft - B.K. and C.U.; Writing, review and editing - B.K. and C.U. with help from all authors.

Funding

The Heinrich Pette Institute, Leibniz Institute for Experimental Virology is supported by the Free and Hanseatic City of Hamburg and the Federal Ministry of Health. C.U. and B.K. are supported by EU Horizon 2020 ERC StG-2017 759661. C.U. and B.K. also received funding through Leibniz Association SAW-2014-HPI-4 grant. The work of J.Z., G.B. and R.M. was supported by grants (to J.Z.) from the Deutsche Forschungsgemeinschaft (SFB 1021, A01; IRTG 1384) and the LOEWE program of the state of Hessen (DRUID, B02).

Supplement:

Table S 1: Mass table. Data from at least three representative native mass spectra were analyzed with MassLynx 4.1 and UniDec. M_{theo} is calculated based on amino acid sequence. Full width half-maximum (FWHM) values derived from main peaks, charge state given in parenthesis. Three data points for calculation of average (Avg) and standard deviation (SD) (only two for PEDV complexes).

	Oligomer	M_{theo} (Da)	Avg M_{exp} ± SD (Da)	Avg FWHM (Da) and charge state	nsp7+8 relative intensity fraction (%)
SARS-CoV-2	nsp7+8 (1:1)	31121	31140 ± 10	62 (11+)	4 ± 2
	nsp7+8 (2:1)	-	-	-	-
	nsp7+8 (2:2)	62242	62300 ± 20	155 (15+)	96 ± 2
SARS-CoV	nsp7+8 (1:1)	31129	31123 ± 2	20 (11+)	2.3 ± 0.2
	nsp7+8 (2:1)	-	-	-	-
	nsp7+8 (2:2)	62258	62267 ± 2	65 (15+)	97.6 ± 0.2
MERS-CoV	nsp7+8 (1:1)	30931	30954.0 ± 0.0	20 (10+)	73 ± 11
	nsp7+8 (2:1)	40012	40025 ± 2	22 (11+)	8 ± 1
	nsp7+8 (2:2)	61898	61920 ± 10	75 (14+)	19 ± 11
PEDV	nsp7+8 (1:1)	30895	30927 ± 1	20 (10+)	52 ± 4
	nsp7+8 (2:1)	40102	40238 ± 3	27 (11+)	6 ± 1
	nsp7+8 (2:2)	61723	61863 ± 1	45 (15+)	42 ± 2
HCoV-229E	nsp7+8 (1:1)	30901	30920 ± 10	20 (10+)	20 ± 7
	nsp7+8 (2:1)	40188	40145 ± 1	29 (11+)	12 ± 1
	nsp7+8 (2:2)	61793	61839 ± 1	45 (15+)	69 ± 6
TGEV	nsp7+8 (1:1)	30930	30962 ± 6	22 (11+)	17 ± 3
	nsp7+8 (2:1)	40401	40470 ± 20	68 (12+)	83 ± 3
	nsp7+8 (2:2)	-	-	-	-
FIPV	nsp7+8 (1:1)	308334	30850 ± 5	26 (11+)	17 ± 2
	nsp7+8 (2:1)	40234	40400 ± 100	208 (12+)	83 ± 2
	nsp7+8 (2:2)	-	-	-	-

Table S 2: Sequence identity matrix of nsp7-8 species. Values for pairwise sequence identity are given in percent. For the multiple sequence alignment with identity matrix output the SIAS Sequence identity and similarity tool has been used provided by Secretaria general de sciencia, technologica e innovacion of Spain (**http://imed.med.ucm.es/Tools/sias.html**). As input parameter, length of the smallest sequence was selected.

%	SARS-CoV-2	SARS-CoV	HCoV-229E	PEDV	FIPV	TGEV	MERS
SARS-CoV-2	100						
SARS-CoV	98	100					
HCoV-229E	43	44	100				
PEDV	42	42	71	100			
FIPV	42	43	63	62	100		
TGEV	42	42	64	61	94	100	
MERS	28	28	21	21	20	20	100

625 **Table S 3: SAXS experimental parameters and analysis methods.**

Data collection parameters	
Instrument	EMBL P12 (PETRAIII, DESY, Hamburg)
beam geometry (mm^2)	0.2 × 0.12
Wavelength (nm)	0.12
S-range (nm^{-1})	0.03 – 5
exposure time (s)	2 (20 × 0.1)
temperature (K)	293
Software employed	
primary data reduction	SASFLOW
data processing	PRIMUS
computation of model intensities	CRYOL
determination of mixture volume fraction	OLIGOMER
rigid body modelling	SASREFMX

626 **Table S 4: Overall parameters computed from the SAXS curves.**

c (mg/mL)	*R*g (nm)	MW Bayes (kDa)	Fit to tetramer T1	Mixture of tetramer and dimer of tetramer		Mixture of tetramer and hexadecamer	
			χ^2	χ^2	Tetramer volume fraction	χ^2	Tetramer volume fraction
1.2	3.25	46	1.35	1.34	1	1.34	1
1.2	3.41	58	1.27	1.27	1	1.27	1
2.1	3.37	56	1.31	1.41	0.97	1.47	1
3.9	3.46	60	2.57	2.54	0.9	3.7	0.98
4.4	3.41	62	1.97	2.2	0.9	3.34	0.97
7.7	3.56	62	5.13	2.3	0.8	4.84	0.95
9.1	3.67	67	14.32	2.45	0.69	9.54	0.91
10.4	3.79	62	22.95	4.4	0.73	15.02	0.93
10.6	3.79	74	21.79	2.86	0.66	12.75	0.91
11.5	3.66	62	4.94	2.14	0.79	4.77	0.94
12.8	3.73	74	62.98	5.13	0.63	30.59	0.9
13.1	3.53	62	19.63	5.29	0.77	15.77	0.94
16.6	3.82	74	17.89	2.27	0.64	9.96	0.9
20	3.67	68	40.19	5.59	0.68	20.25	0.91
21.1	3.82	74	67.56	4.62	0.61	29.52	0.89
25.8	3.8	74	73	4.69	0.57	27.08	0.88
26.6	3.86	74	58.68	6.49	0.62	24.02	0.89
31.1	3.91	83	148.76	7.82	0.52	45.67	0.86
32.1	3.82	76	111.04	10.92	0.61	41.36	0.89
47.7	3.95	86	86.73	6.57	0.47	21.69	0.84

627

628 **Table S 5: Results table, overview of main experimental results for nsp7+8 complexes of seven CoV species.**
629 Results from left to right: Categorization of complexes, quantitation of complexes by native MS (values are given
630 in percent), Identified homodimers nsp72 and nsp82, and dimerization of precursor (clearly assigned species
631 indicated with "yes" and if no assignment possible with minus(-)), nsp8 and nsp7 possible mutations that shift
632 heterotrimer to heterotetramer ratio.

	Group	Complex nsp7+8 (1:1)	Complex nsp7+8 (2:1)	Complex nsp7+8 (2:2)	Dimer nsp7 (2)	Dimer nsp8 (2)	Dimer nsp7-8	nsp8 Glu77/ Asn78	nsp7 Phe76
SARS-CoV-2	A	4	-	96	yes	yes	yes	Glu77	-
SARS-CoV	A	2	-	98	yes	yes	yes	Glu77	-
MERS-CoV	AB	73	8	19	yes	-	*different precursor	Glu77	Phe76
HCoV-229E	AB	20	12	69	yes	-	yes	Asn78	Phe76
PEDV	AB	52	6	42	yes	-	yes	Asn78	Phe76
FIPV	B	17	83	-	yes	-	-	-	Phe76
TGEV	B	17	83	-	yes	-	-	-	Phe76

633

634

Table S 6: Amino acid sequences of precursor constructs.

>SARS-CoV-2_nsp7-8-His$_6$ SKMSDVKCTSVVLLSVLQQLRVESSSKLWAQCVQLHNDILLAKDTTEAFEKMVSLLSVLLSMQGAVDINKLCEEMLDNRATLQAI ASEFSSLPSYAAFATAQEAYEQAVANGDSEVVLKKLKKSLNVAKSEFDRDAAMQRKLEKMADQAMTQMYKQARSEDKRAKVTS AMQTMLFTMLRKLDNDALNNIINNARDGCVPLNIIPLTTAAKLMVVIPDYNTYKNTCDGTTFTYASALWEIQQVVDADSKIVQLSEIS MDNSPNLAWPLIVTALRANSAVKLQ**SGSGSARGSHHHHHH**
>SARS-CoV_nsp7-8-His$_6$ SKMSDVKCTSVVLLSVLQQLRVESSSKLWAQCVQLHNDILLAKDTTEAFEKMVSLLSVLLSMQGAVDINRLCEEMLDNRATLQAI ASEFSSLPSYAAYATAQEAYEQAVANGDSEVVLKKLKKSLNVAKSEFDRDAAMQRKLEKMADQAMTQMYKQARSEDKRAKVTS AMQTMLFTMLRKLDNDALNNIINNARDGCVPLNIIPLTTAAKLMVVVPDYGTYKNTCDGNTFTYASALWEIQQVVDADSKIVQLSEI NMDNSPNLAWPLIVTALRANSAVKLQ**SARGSHHHHHH**
>HCoV-229E_nsp7-8-His$_6$ SKLTDLKCTNVVLMGILSNMNIASNSKEWAYCVEMHNKINLCDDPETAQELLLALLAFFLSKHSDFGLGDLVDSYFENDSILQSVA SSFVGMPSFVAYETARQEYENAVANGSSPQIIKQLKKAMNVAKAEFDRESSVQKKINRMAEQAAAAMYKEARAVNRKSKVVSA MHSLLFGMLRRLDMSSVDTILNMARNGVVPLSVIPATSAARLVVVVPDHDSFVKMMVDGFVHYAGVVWTLQEVKDNDGKNVHL KDVTKENQEILVWPLILTCERVVKLQ**SGSGHHHHHH**
>PEDV_nsp7-8-His$_6$ SKLTDIKCSNVVLLGCLSSMNVSANSTEWAYCVDLHNKINLCNDPEKAQEMLLALLAFFLSKNSAFGLDDLLESYFNDNSMLQSV ASTYVGLPSYVIYENARQQYEDAVNNGSPPQLVKQLRHAMNVAKSEFDREASTQRKLDRMAEQAAAQMYKEARAVNRKSKVV SAMHSLLFGMLRRLDMSSVDTILNLAKDGVVPLSVIPAVSATKLNIVTSDIDSYNRIQREGCVHYAGTIWNIIDIKDNDGKVVHVKEV TAQNAESLSWPLVLGCERIVKLQ**SGSGHHHHHH**
>FIPV_nsp7-8-His$_6$ SKLTEMKCTNVVLLGLLSKMHVESNSKEWNYCVGLHNEINLCDDPDAVLEKLLALIAFFLSKHNTCDLSDLIESYFENTTILQSVAS AYAALPSWIAYEKARADLEEAKKNDVSPQLLKQLTKACNIAKSEFEREASVQKKLDKMAEQAAASMYKEARAVDRKSKIVSAMHS LLFGMLKKLDMSSVNTIIEQARNGVLPLSIIPAASATRLIVVTPNLEVLSKVRQENNVHYAGAIWSIVEVKDANGAQVHLKEVTAAN ELNITWPLSITCERTTKLQ**SGSGHHHHHH**
>TGEV_nsp7-8-His$_6$ SKLTEMKCTNVVLLGLLSKMHVESNSKEWNYCVGLHNEINLCDDPEIVLEKLLALIAFFLSKHNTCDLSELIESYFENTTILQSVASA YAALPSWIALEKARADLEEAKKNDVSPQILKQLTKAFNIAKSDFEREASVQKKLDKMAEQAAASMYKEARAVDRKSKIVSAMHSLL FGMLKKLDMSSVNTIIDQARNGVLPLSIIPAASATRLVVITPSLEVFSKIRQENNVHYAGAIWTIVEVKDANGSHVHLKEVTAANELN LTWPLSITCERTTKLQ**SGSGHHHHHH**
>MERS-CoV_nsp7-11-His$_6$ SKLTDLKCTSVVLLSVLQQLHLEANSRAWAFCVKCHNDILAATDPSEAFEKFVSLFATLMTFSGNVDLDALASDIFDTPSVLQATL SEFSHLATFAELEAAQKAYQEAMDSGDTSPQVLKALQKAVNIAKNAYEKDKAVARKLERMADQAMTSMYKQARAEDKKAKIVSA MQTMLFGMIKKLDNDVLNGIISNARNGCIPLSVIPLCASNKLRVVIPDFTVWNQVVTYPSLNYAGALWDITVINNVDNEIVKSSDVV DSNENLTWPLVLECTRASTSAVKLQNNEIKPSGLKTMVVSAGQEQTNCNTSSLAYYEPVQGRKMLMALLSDNAYLKWARVEGK DGFVSVELQPPCKFLIAGPKGPEIRYLYFVKNLNNLHRGQVLGHIAATVRLQAGSNTEFASNSSVLSLVNFTVDPQKAYLDFVNAG GAPLTNCVKMLTPKTGTGIAISVKPESTADQETYGGASVCLYCRAHIEHPDVSGVCKYKGKFVQIPAQCVRDPVGFCLSNTPCNV CQYWIGYGCNCDSLRQAALPQ**SKDSNFLNHHHHHH**

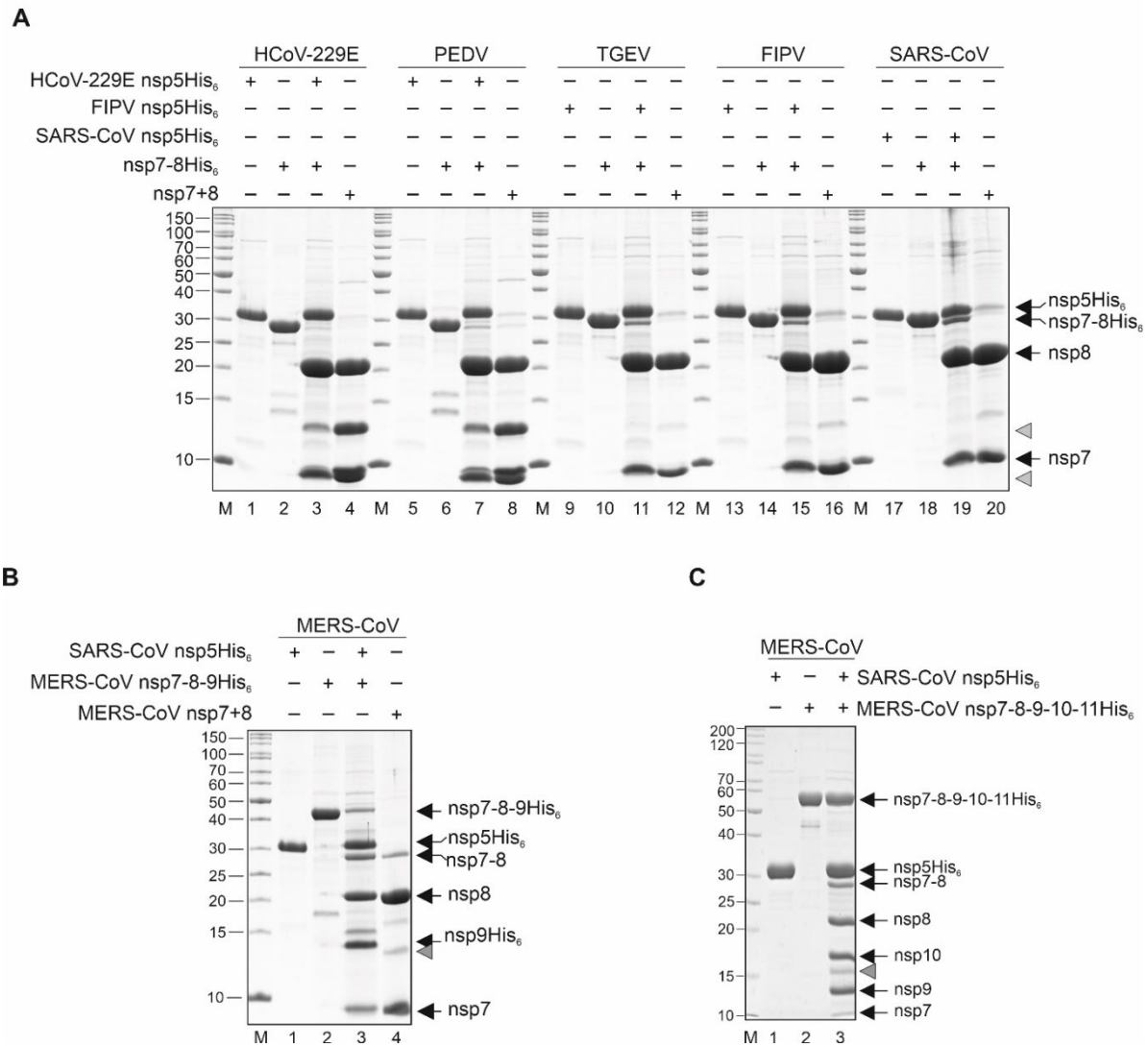

Figure S 1: Mpro mediated processing of precursor protein constructs. SDS-PAGE analysis of M^{pro} (nsp5)-mediated processing and generation of coronavirus nsp7+8 complexes with authentic *N*- and *C*-termini from polyprotein precursors nsp7-8, nsp7-8-9 and nsp7-11. The nsp7+8 complexes of HCoV-229E, PEDV, FIPV, TGEV, and SARS-CoV were produced from the respective nsp7-8-His_6 precursors and MERS-CoV was produced from an nsp7-9-His_6 precursor. Precursor proteins were purified by Ni^{2+}-IMAC and ion-exchange chromatography. Then, 15 µg protein was cleaved with M^{pro} (nsp5-His_6, 5 µg) for 48 h at 4 °C. Subsequently, His_6-tag containing cleavage products were removed by passing the material through a Ni^{2+}-IMAC column and nsp7+8 complexes were enriched by ion-exchange chromatography. (**A**) SDS-PAGE showing the purified M^{pro} (nsp5-His_6) – lanes 1, 5, 9, 13, 17; nsp7-8- His_6 – lanes 2, 6, 10, 14, 18; M^{pro}-mediated cleavage reaction – lanes 3, 7, 11, 15, 19; enriched nsp7+8 complexes – lanes 4, 8, 12, 16, 20. (**B**) SDS-PAGE showing the purified M^{pro} (nsp5-His_6) – lane 1; nsp7-8-9-His_6 – lane 2; M^{pro}-mediated cleavage reaction – lane 3; enriched nsp7+8 complex – lane 4. (**C**) SDS-PAGE showing the purified M^{pro} (nsp5-His_6) – lane 1; nsp7-8-9-10-11-His_6 – lane 2; M^{pro} mediated cleavage reaction – lane 3. Lane M, marker proteins with molecular masses in kD indicated to the left. Black arrows on the right indicate the identities of proteins generated from precursor proteins by M^{pro}-mediated cleavage. Gray arrowheads indicate aberrant *in vitro* cleavage products of nsp8 as observed previously for SARS-CoV [22]. nsp – nonstructural protein. +/– indicate the presence or absence of the respective proteins.

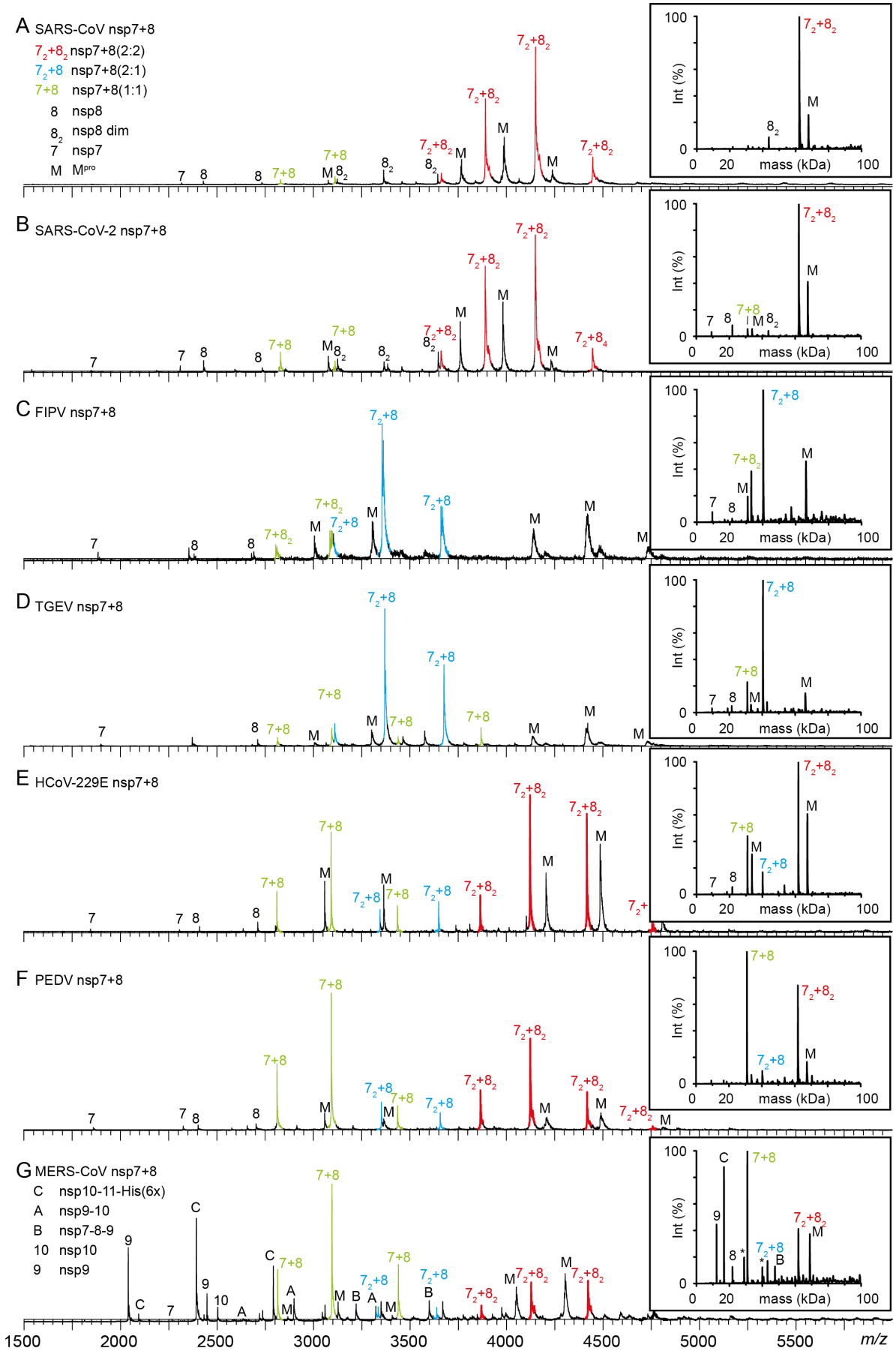
A SARS-CoV nsp7+8
7_2+8_2 nsp7+8(2:2)
7_2+8 nsp7+8(2:1)
7+8 nsp7+8(1:1)
8 nsp8
8_2 nsp8 dim
7 nsp7
M M^{pro}
B SARS-CoV-2 nsp7+8
C FIPV nsp7+8
D TGEV nsp7+8
E HCoV-229E nsp7+8
F PEDV nsp7+8
G MERS-CoV nsp7+8
C nsp10-11-His(6x)
A nsp9-10
B nsp7-8-9
10 nsp10
9 nsp9
Int (%)
mass (kDa)
m/z
1500
2000
2500
3000
3500
4000
4500
5000
5500

655

656 **Figure S 2: Native MS of nsp7+8 complexes of seven CoVs representing five different CoV species.**
657 Representative mass spectra showing distinct nsp7+8 complexation patterns that were classified into the three
658 groups A, B and AB. Complex formation triggered by M^{pro} (M) mediated cleavage of 15 µM nsp7-8-His_6 or MERS-
659 CoV nsp7-11-His_6 precursors in 300 mM AmAc, 1 mM DTT, pH 8.0. (**A**) SARS-CoV-2 and (**B**) SARS-CoV from
660 group A forming nsp7+8 (2:2) heterotetramers (red), (**C**) FIPV and (**D**) TGEV from group B forming nsp7+8 (2:1)
661 heterotrimers (blue) as well as (**E**) HCoV-229E and (**F**) PEDV from group AB forming both complex
662 stoichiometries. (**G**) MERS-CoV, also from group AB, produced from an nsp7-11 precursor, additionally results in
663 several processing intermediates that allow for an estimation of relative cleavage efficiencies at different cleavage
664 sites. All groups form nsp7+8 (1:1) heterodimers as intermediate state (green).

665

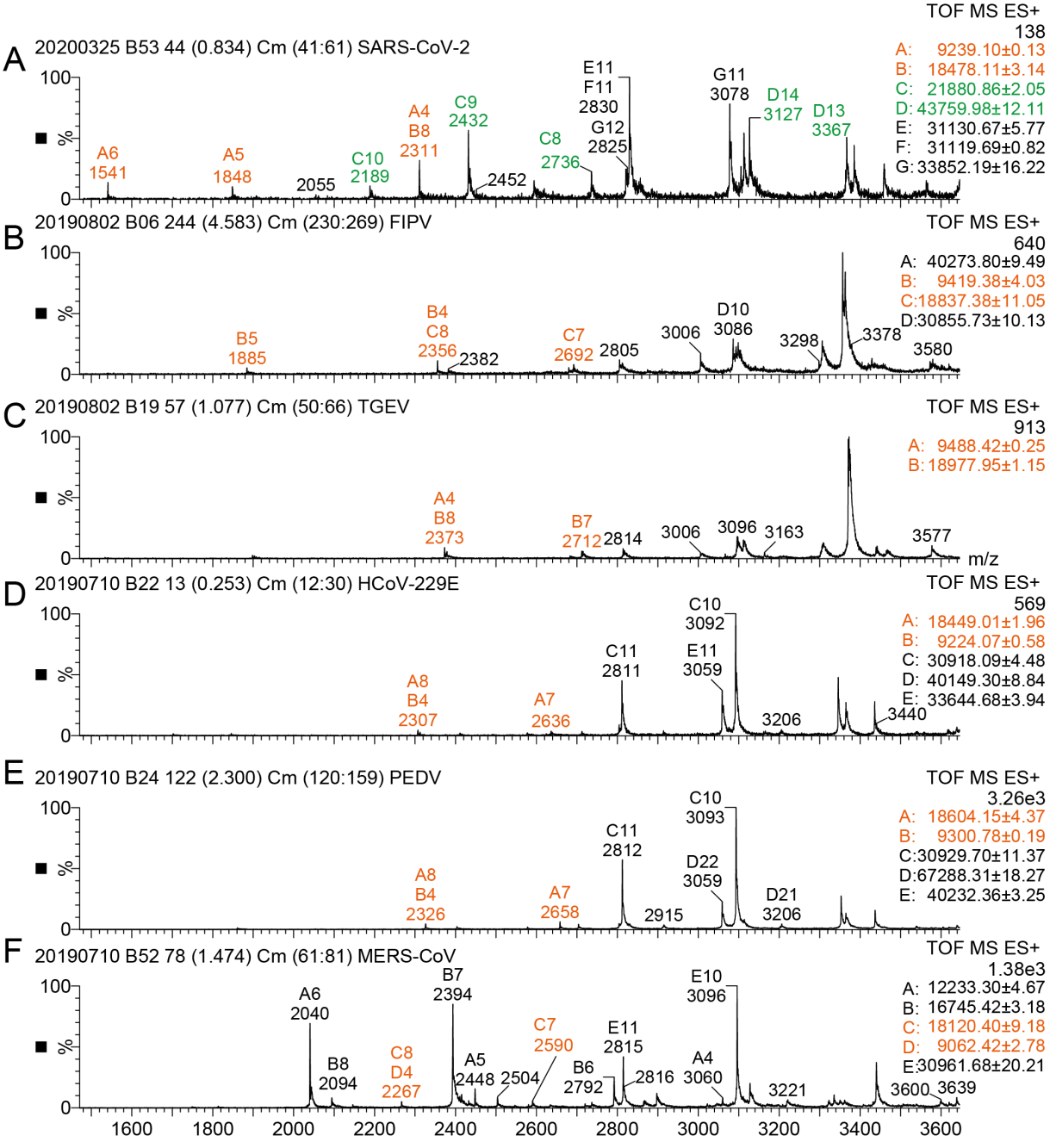

Figure S 3: Zoom in on nsp7 and nsp8 monomers and homodimers from spectra in Figure S 2. Representative native mass spectra showing region 1500-3600 *m/z* (for full spectra see Figure S 2) of cleaved nsp7-8 or nsp7-11 precursors showing that homodimers of nsp8 (green $nsp8_2$) were detected for SARS-CoV-2 (**A**) and SARS-CoV (Figure S 2), but not from (**B**) FIPV, (**C**) TGEV, (**D**) HCoV-229E, (**E**) PEDV and (**F**) MERS-CoV. Homodimers of nsp7 (orange, $nsp7_2$) were detected for all seven CoVs.

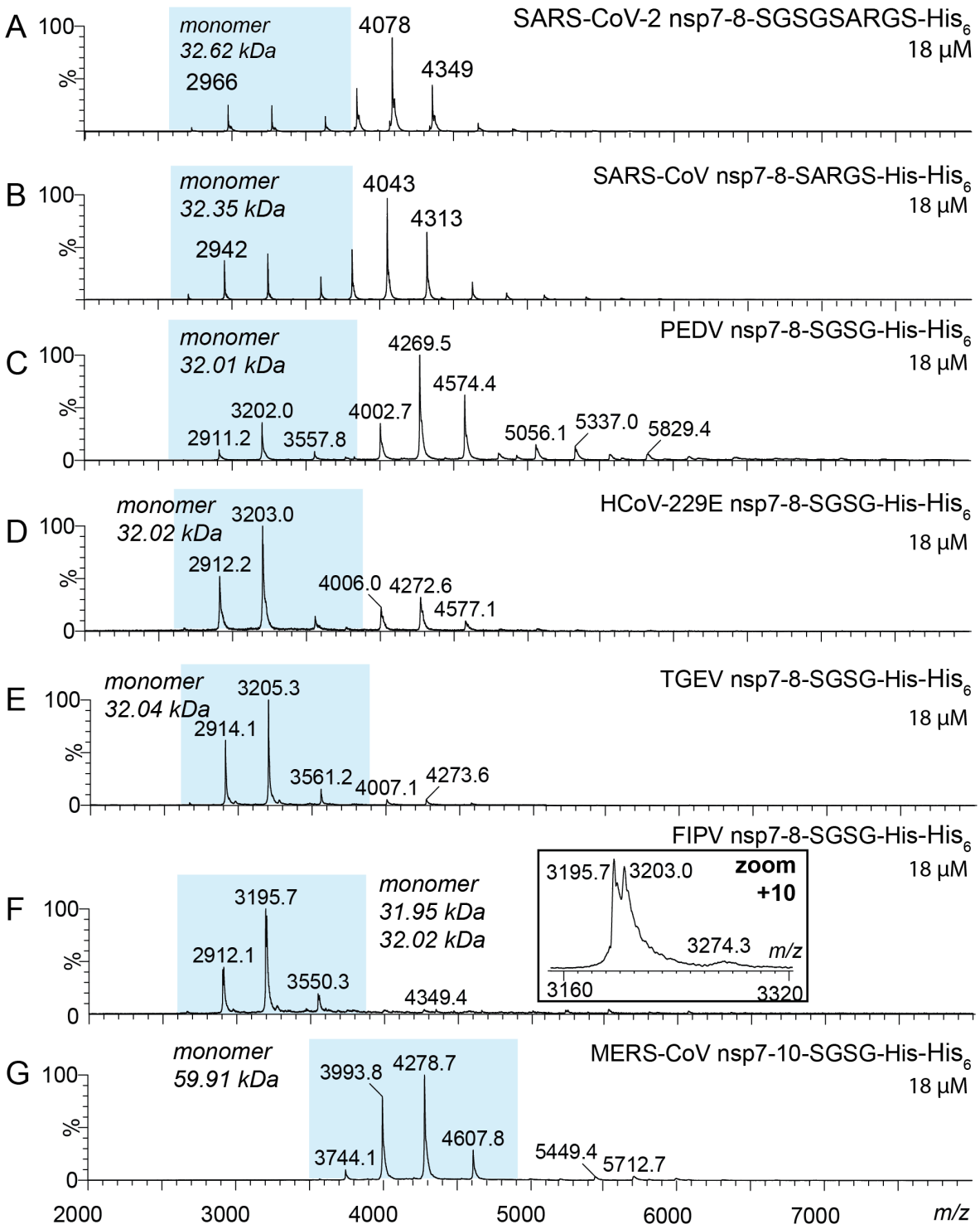

Figure S 4: Mass and oligomeric state of nsp7-8 precursors. Native MS of nsp7-8 precursors (**A-G**) sprayed at 18 µM from 300 mM AmAc, pH 8.0 and 1 mM DTT. Dominant charge envelope is highlighted (blue box). Labelled are *m/z* values and mass of the main oligomers. (**F**) Inset shows mass heterogeneity in FIPV nsp7-8. The experimental molecular weight M_{exp} of the precursors agrees with the sequence-derived theoretical M_{theo} (Table S 1). Only FIPV nsp7-8 contained two mass species separated by ~110 Da. This heterogeneity was attributed to the precursor's central nsp8 domain following M^{pro} processing. Assignment to an amino acid variation failed but potentially was the result of codon heterogeneity in the plasmid. Nevertheless, both forms behaved identical and we refrained from further optimization.

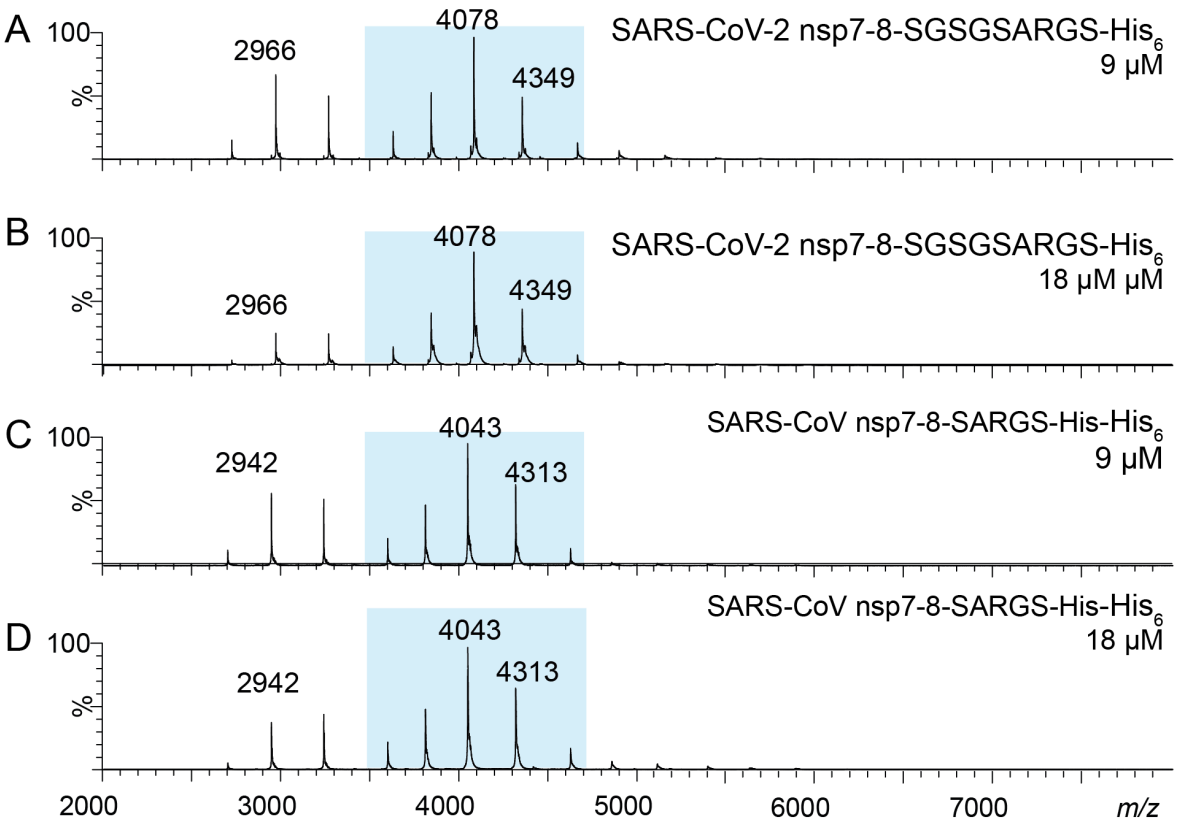

682

683 **Figure S 5: Monomer-dimer equilibrium in SARS-CoV and SARS-CoV nsp7-8 precursors.** Native mass spectra
684 of nsp7-8 precursors of SARS-CoV-2 (**A**) 18 µM and (**B**) 9 µM and SARS-CoV (**C**) 18 µM and (**D**) 9 µM. Proteins at
685 18 µM were diluted to 9 µM, incubated for 10 min and then sprayed from 300 mM AmAc, pH 8.0 and 1 mM DTT.
686 Labeled are *m*/*z* values.

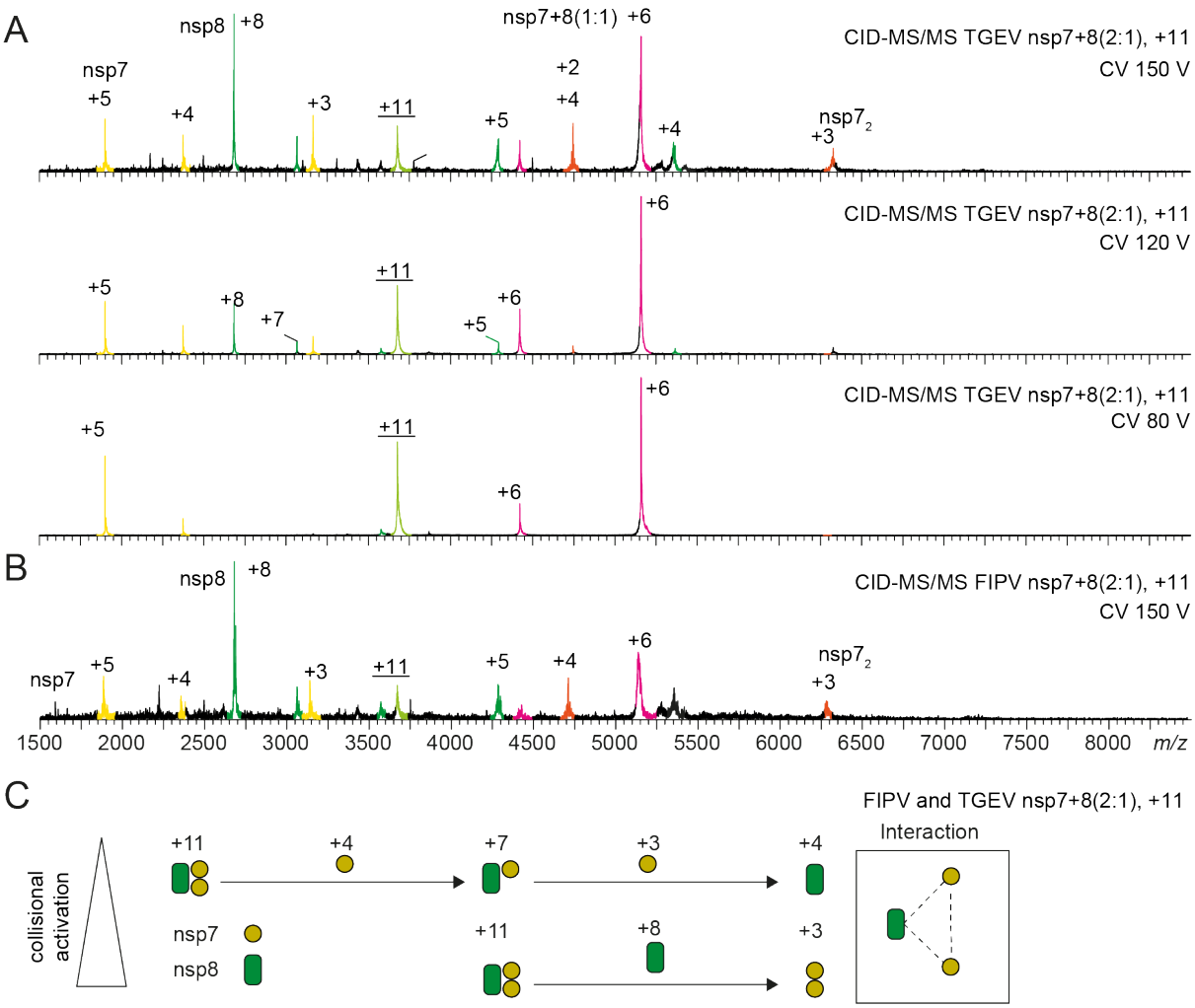

Figure S 6: Topological reconstruction from CID-MS/MS of FIPV and TGEV nsp7+8 heterotrimers. (**A**) Three product ion spectra of the TGEV 11+ nsp7+8 (2:1) heterotrimer at different collisional voltages (CV). Increased collisional activation allows assignment of additional charge states and product species. (**B**) Product ion spectra of the FIPV 11+ nsp7+8 (2:1) show a similar dissociation pattern as its homologue from TGEV. (**C**) Schematic pathway of dissociation allows for a topological reconstruction of the TGEV and FIPV heterotrimers.

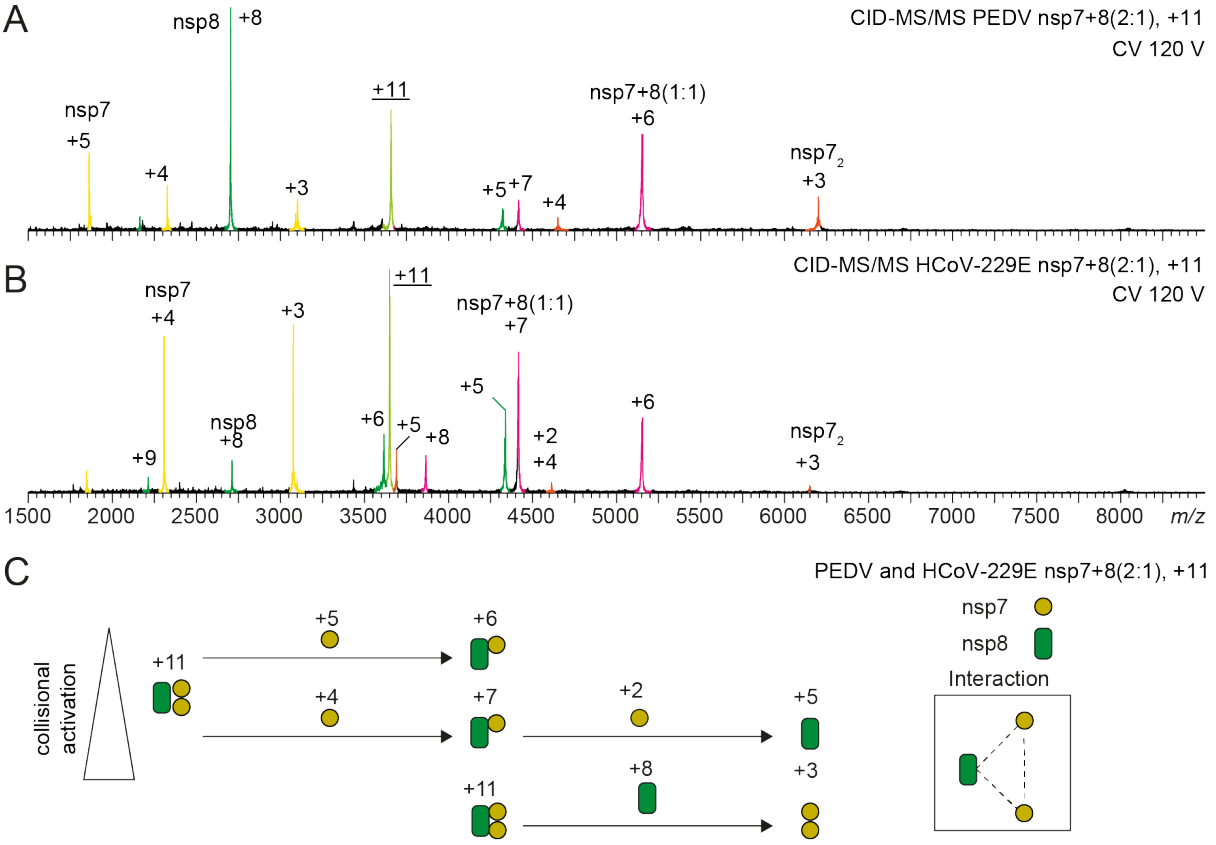

Figure S 7: Topological reconstruction from CID-MS/MS of PEDV and HCoV-229E nsp7+8 heterotrimers. (**A**) Product ion spectra of the PEDV 11+ nsp7+8 (2:1) heterotrimer shows nsp7 homodimeric species, revealing the core interaction of this protein complex. (**B**) Product ion spectra of the HCoV-229E 11+ nsp7+8 (2:1) heterotrimer. Compared to the dissociation pattern of PEDV homologue, the HCoV-229E nsp7 and nsp8 high charge products have distinct intensities and charge state distributions but the detected product species are similar. (**C**) Schematic pathway of dissociation allows for a topological reconstruction of the PEDV and HCoV-229E heterotrimer.

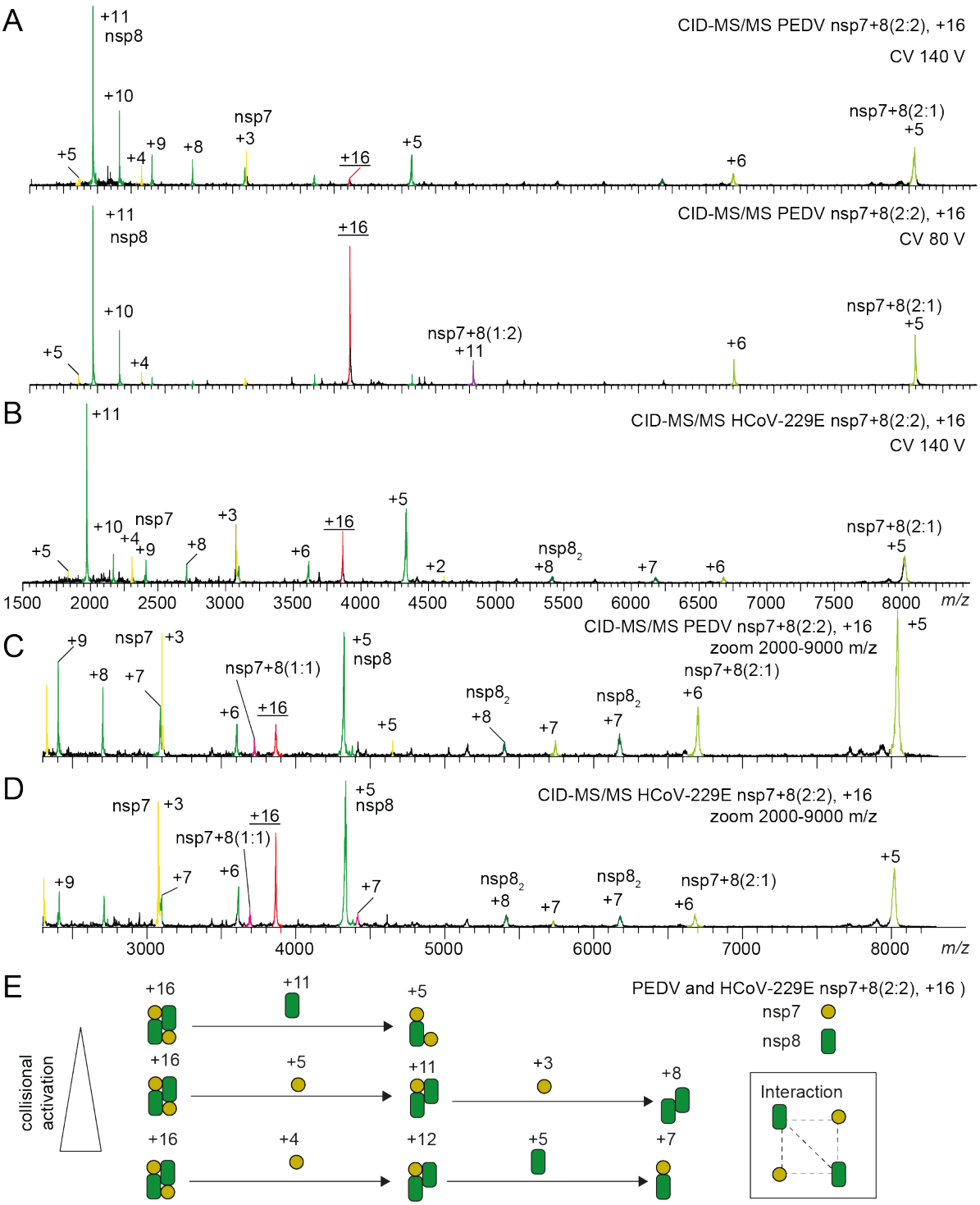

Figure S 8: Topological reconstruction from CID-MS/MS of PEDV and HCoV-229E nsp7+8 heterotetramers. (**A**) Product ion spectra of the PEDV 16+ nsp7+8 (2:2) heterotetramer at two different CV. At 80 V CV, the dissociation of one nsp7 or alternatively one nsp8 occurs, as indicated by the high and low charge products. Notably, the high charge state of the dissociated nsp8 suggests an extended shape of the ion. At 140 V CV, nsp8 dissociates at lower charge states suggesting alternative dissociation pathways. (**B**) Product ion spectra of HCoV-229E 16+ nsp7+8 (2:2) heterotetramer at 140 V similar to the PEDV heterotetramer. (**C** and **D**) The zoom (2000-9000 *m/z*), excluding the nsp8 high charge states, reveals additional product species (e.g. the nsp8$_2$ homodimer). (**E**) Schematic pathway of dissociation allows for a topological reconstruction of the PEDV and HCoV-229E heterotetramer.

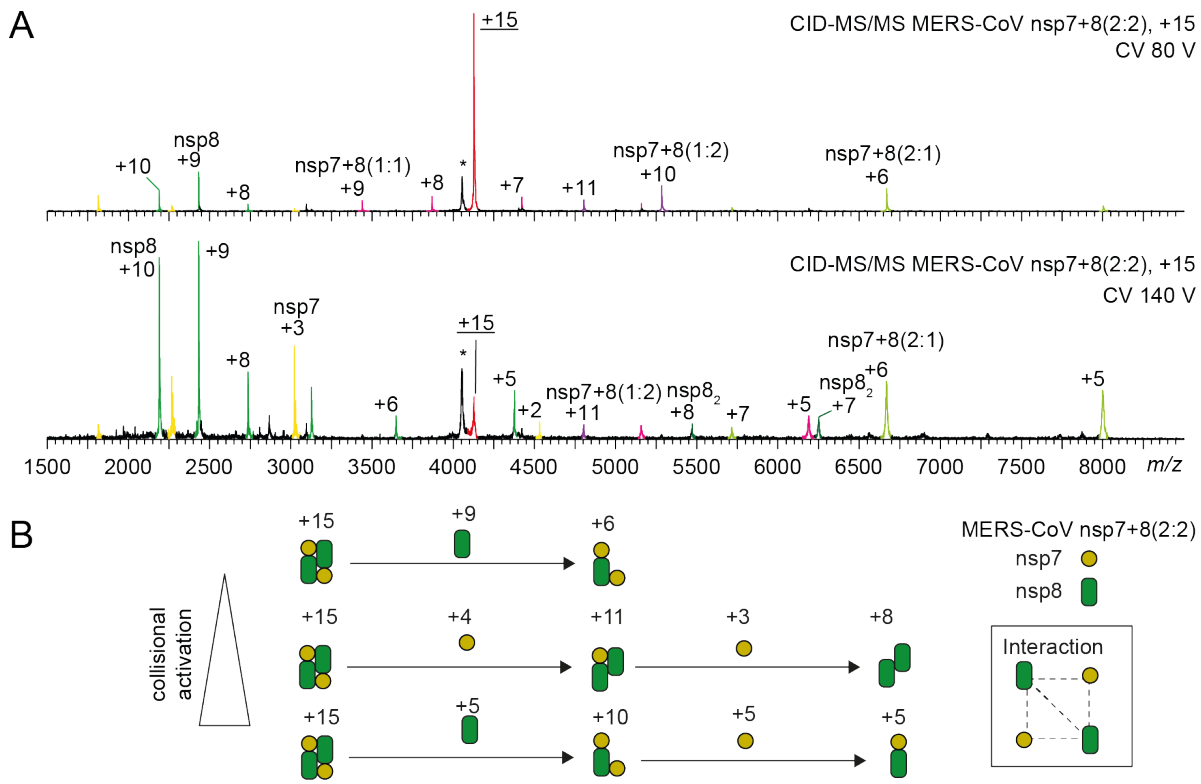

Figure S 9: Topological reconstruction from CID-MS/MS of MERS-CoV nsp7+8 heterotetramers. (**A**) Product ion spectra of MERS-CoV 15+ nsp7+8 (2:2) heterotetramer at two different CV. At 100 V CV, the dissociation of one nsp7 or, alternatively, one nsp8 occurs as indicated by the high and low charge products. At 140 V CV, other dissociation products increase in intensity (e.g. $nsp8_2$ homodimer and nsp7+8(1:1) heterodimer). (**B**) Schematic pathway of dissociation allows topological reconstruction of the MERS-CoV heterotetramers.

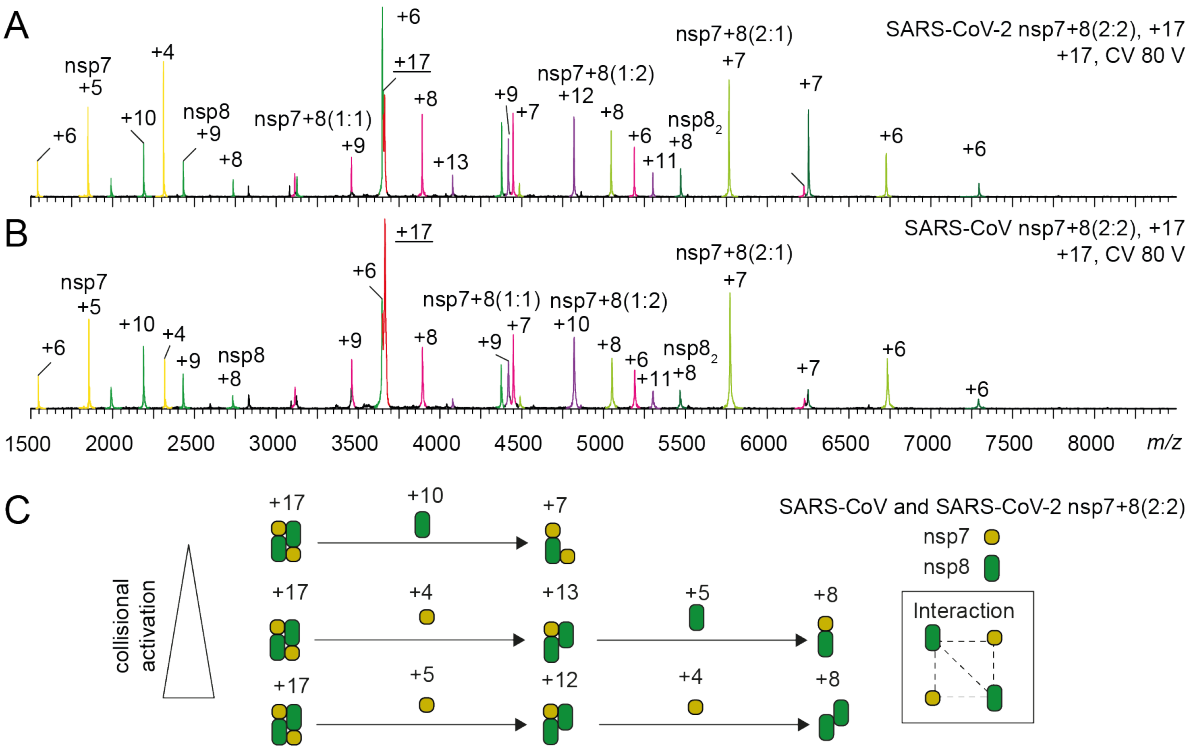

Figure S 10: Topological reconstruction from CID-MS/MS of SARS-CoV and SARS-CoV-2 nsp7+8 heterotetramers. Product ion spectra of (**A**) SARS-CoV-2 and (**B**) SARS-CoV 17+ nsp7+8 (2:2) heterotetramers are shown. High charge state precursor allows for efficient dissociation already at relatively low activation (CV 80 V). Product ion species can be clearly assigned from the overview spectra. (**C**) Schematic pathway of dissociation allows topological reconstruction of the SARS-CoV-2 and SARS-CoV heterotetramers.

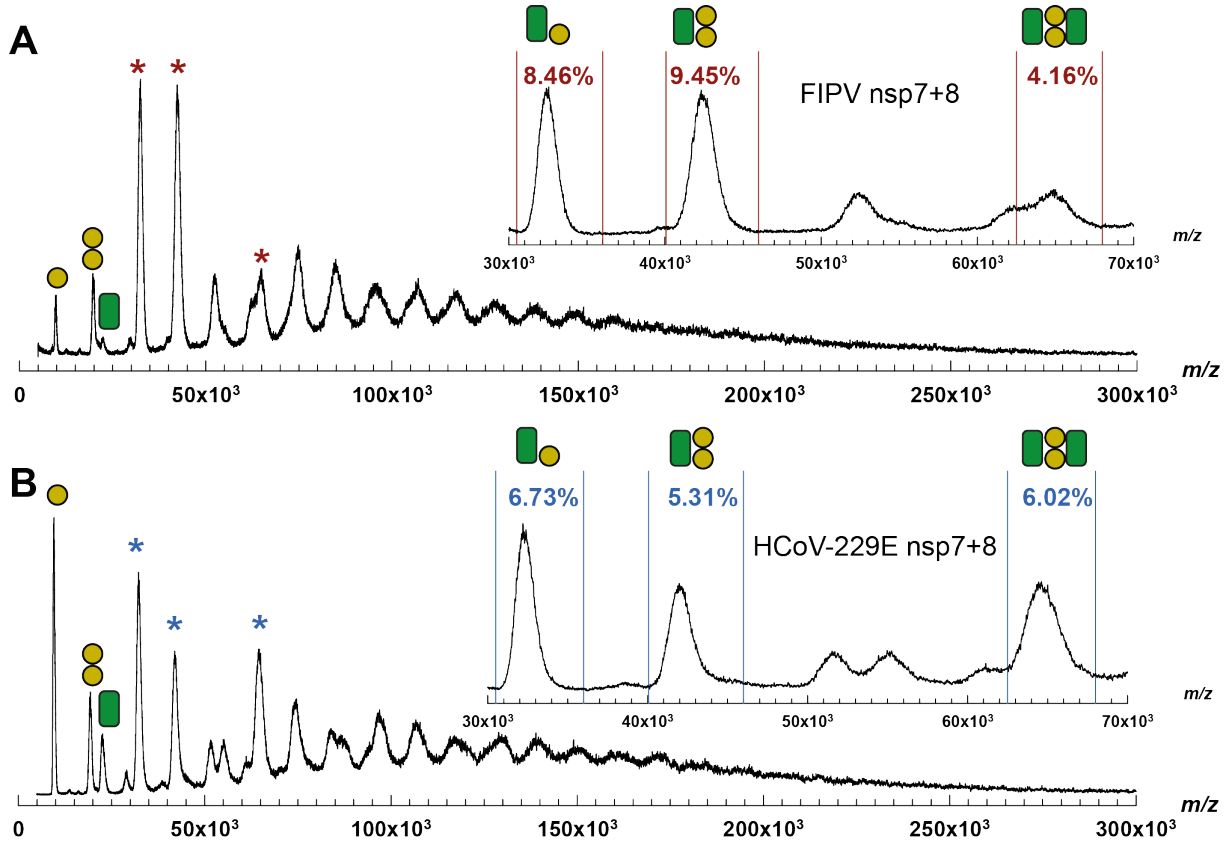

Figure S 11: MALDI-MS of nsp7+8 complexes from FIPV and HCoV-229E stabilized with crosslinker. (**A**) MALDI mass spectrum of FIPV nsp7+8 crosslinked with 0.15 % glutaraldehyde for 25 min at 4 °C. Inset shows the most abundant nsp7+8 complexes: (1:1) heterodimer (32.4 kDa) and (2:1) heterotrimer (42.5 kDa). Abundance is determined from relative peak areas as indicated (red). (**B**) MALDI mass spectrum of HCoV-229E nsp7+8 crosslinked with 0.15 % glutaraldehyde for 25 min at 4 °C. Inset shows most abundant nsp7+8 complexes: (1:1) heterodimer (32.2 kDa) and (2:2) heterotetramer (64.6 kDa). Abundance is determined from relative peak areas as indicated (blue). Symbols depict stoichiometry of mass species of nsp7 (yellow) and nsp8 (green) with highest signal strength. Masses are higher in crosslinked samples due to the additional glutaraldehyde molecules. Mass spectra were not calibrated. Each spectrum shown was generated from three MALDI spots. Most signals, except for the HCoV-229E heterotetramer, above 50,000 *m/z* are low abundant and likely due to over-crosslinking.

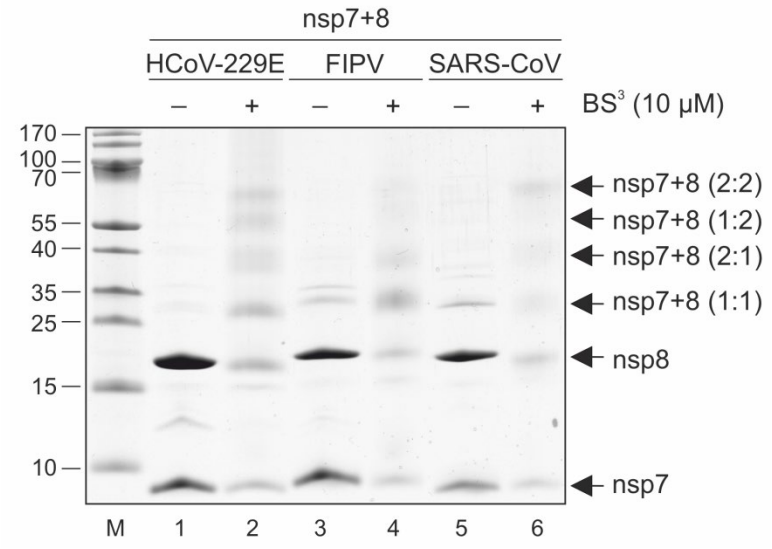

Figure S 12: SDS-PAGE analysis of chemically cross-linked HCoV-229E, FIPV, and SARS-CoV nsp7+8 complexes. The 5 μg protein of nsp7+8 complexes were crosslinked with 10 μM BS^3 (ThermoFisher) in reaction buffer (20 mM HEPES-KOH, pH 8.0, 30 mM KCl, and 2 mM β-mercaptoethanol). Crosslinking was carried out at 37 °C for 30 min and quenched with 50 mM AmAc for another 30 min at 37 °C. After terminating the crosslinking reaction, the samples were mixed with an excess of Laemmli sample buffer (50 mM Tris-HCl, pH 6.8, 2.5 % (*w*/*v*) SDS, 10 % (*v*/*v*) glycerol, and 0.01 % (*w*/*v*) bromophenol blue) and analyzed on 12 % SDS-PAGE. Lanes 1, 3, 5 – nsp7+8 complexes not treated with BS^3 (-) and lanes 2, 4, 6 – nsp7+8 complexes treated with BS^3. Lane M, marker proteins; molecular masses in kD are indicated to the left. Black arrows on the right indicate the different oligomeric states of the nsp7+8 complexes obtained by crosslinking.

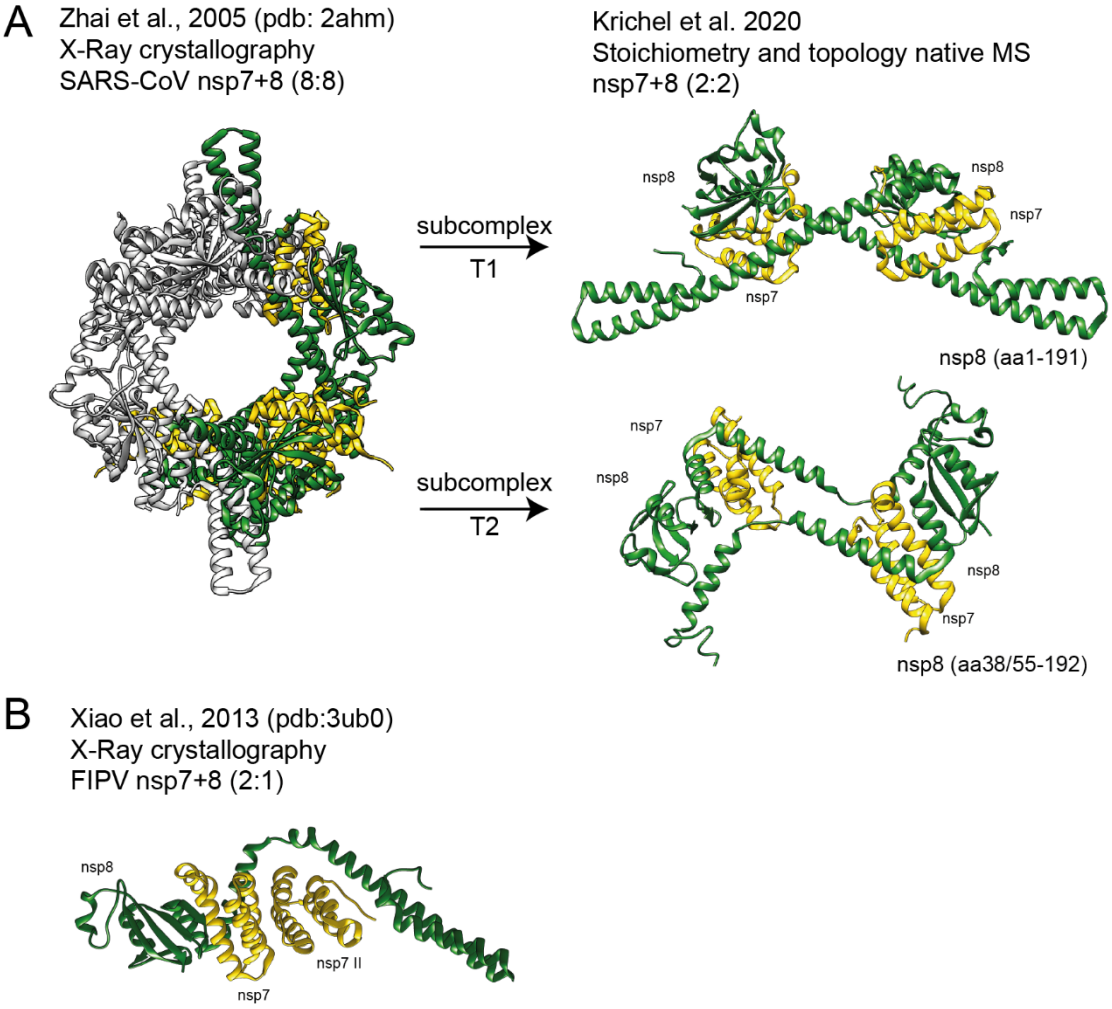

Figure S 13: Candidate structures in agreement with the observed stoichiometries and topologies observed. (**A**) For the full-length heterotetramer, an isolated structure does not exist. However from the larger SARS-CoV nsp7+8 hexadecamer [20] (pdb 2ahm), two conformer subcomplexes of nsp7+8 (2:2), T1 and T2, can be extracted. Both conformers constitute a head-to-tail interaction of two heterodimers by an nsp8:nsp8 interface. Notably, nsp8 in T1 is more extended, containing an almost full-length amino acid sequence (2-193), while in T2 the nsp8 *N*-terminal 35 to 55 residues are unresolved. (**B**) For the trimeric complexes, the only deposited structure is FIPV nsp7+8 (2:1) trimer [21] (pdb 3ub0), which agrees well with our experimental topology.

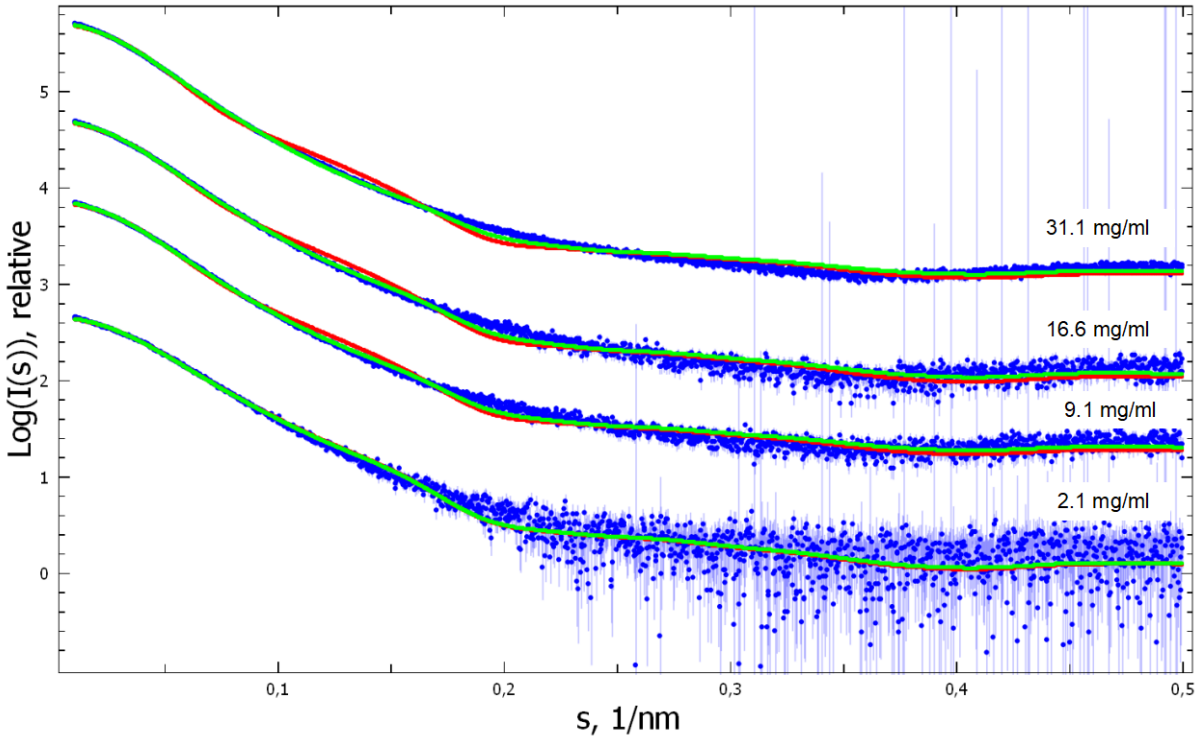

Figure S 14: Fits to all SAXS data. Experimental data (blue with experimental errors) for SARS-CoV-2 nsp7+8 complexes fitted with a mixture of T1 and hexadecamer (red), or T1 and dimer of T1 (green).

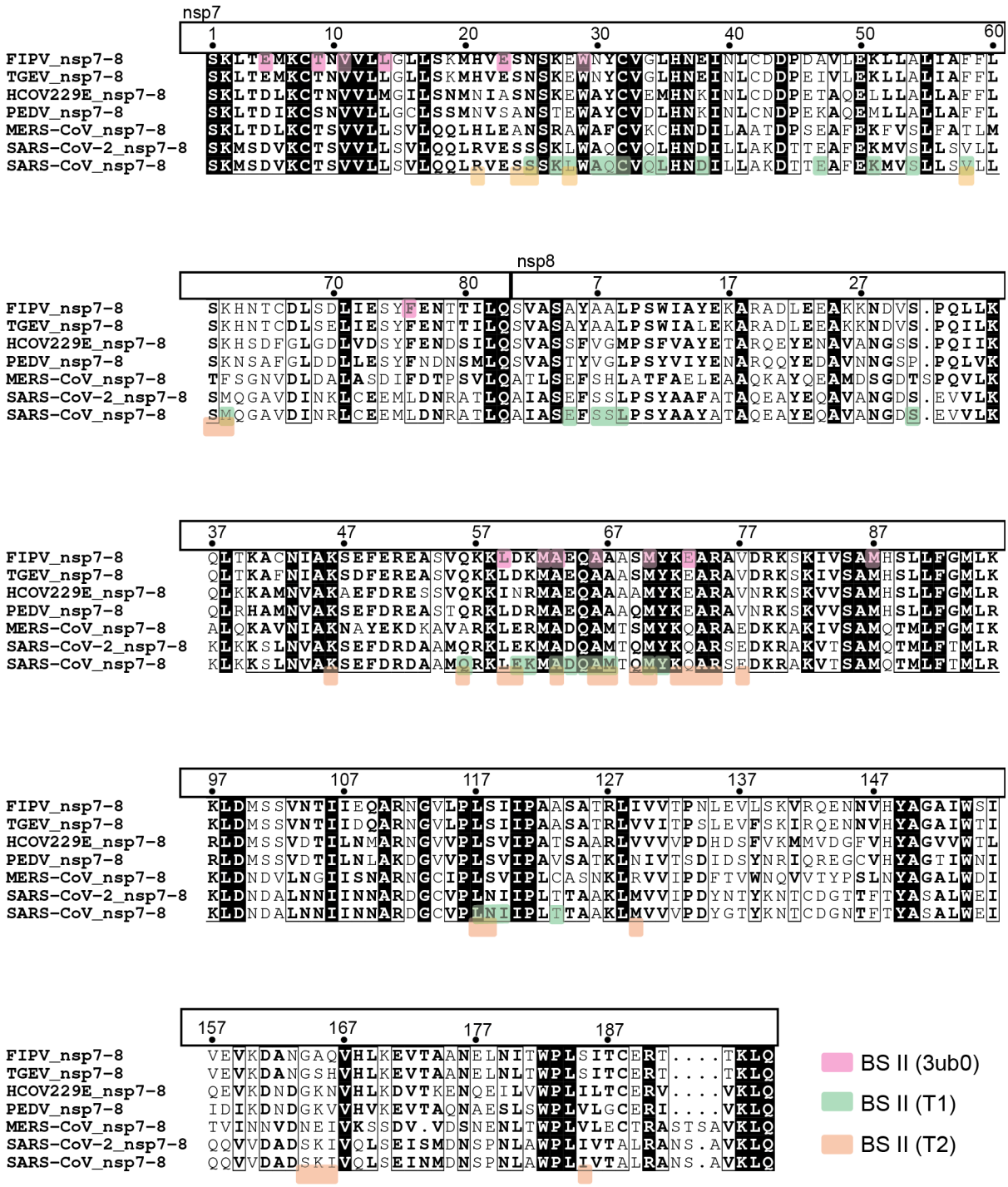

Figure S 15: Sequence alignment of nsp7 and nsp8 from seven CoV species. The multiple sequence alignment of nsp7-8 sequences of the seven tested CoVs is genrated with Clustal Omega [43] and converted by ESPript [44] - http://espript.ibcp.fr using the amino acid sequences without C-terminal linkers and His_6 as input (Table S 6). Highlighted are conserved (black) and semi-conserved (bold) sequences. Further highlighted are molecular contacts at binding site (BS) II in the SARS-CoV nsp7+8 (2:2) heterotetramer candidate structures T1 (green) and T2 (orange) (subcomplexes of pdb 2ahm) as well as in the FIPV nsp7+8 (2:2) heterotrimer (pink, pdb 3ub0). Contacts (VDW radius -0.4 Å) was analyzed with ChimeraX [45].

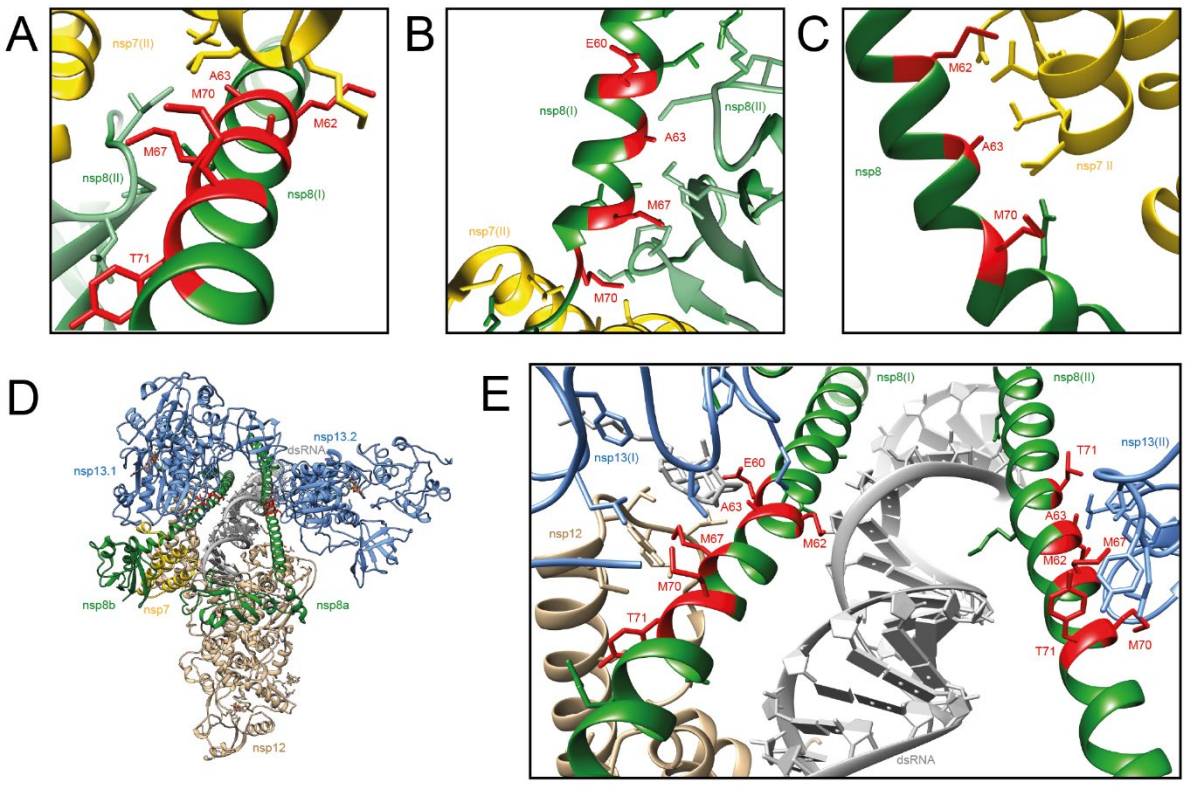

Figure S 16: Conserved stretch of nsp8 has various binding contexts. Candidate complexes involving similar conserved residues (red) in the nsp8 BS II are shown here for (**A**) the SARS-CoV nsp7+8 (2:2) heterotetramer candidate structures T1 and (**B**) T2 (subcomplexes of pdb 2ahm) as well as (**C**) the FIPV nsp7+8 (2:2) heterotrimer (pdb 3ub0). (**D**) Cryo electron microscopy structure of the nsp7+8+12+13 (1:2:1:1) polymerase complex (pdb 6xez) [29]. The two subunits of nsp8 (green), bind as a monomer nsp8a and as a nsp7+nsp8b heterodimer to the nsp12 RdRp. From there, nsp8a and nsp8b extend and interact as a facet with the RNA duplex and also individually with one subunit of the nsp13 helicase. The molecular contacts between nsp8 and nsp12/13 are mediated by exactly the same amino acids in the nsp8 BS II that are involved in nsp7+8 complex formation. (**E**) Zoom into the interacting region at nsp8a and nsp8b BS II and its amino acids in contact (VDW radius -0.4 Å) with the nsp12 thumb domain (brown), nsp13.1 and nsp13.2 (blue). All side chains of residues involved in contacts are displayed. Molecular graphics and analyses performed with UCSF ChimeraX, developed by the Resource for Biocomputing, Visualization, and Informatics at the University of California, San Francisco, with support from National Institutes of Health R01-GM129325 and the Office of Cyber Infrastructure and Computational Biology, National Institute of Allergy and Infectious Diseases [45].

1. References

1. Cui, J., F. Li, and Z.-L. Shi, *Origin and evolution of pathogenic coronaviruses.* Nature Reviews Microbiology, 2019. **17**(3): p. 181-192.
2. Zaki, A.M., et al., *Isolation of a novel coronavirus from a man with pneumonia in Saudi Arabia.* New England Journal of Medicine, 2012. **367**(19): p. 1814-1820.
3. Drosten, C., et al., *Identification of a novel coronavirus in patients with severe acute respiratory syndrome.* New England Journal of Medicine, 2003. **348**(20): p. 1967-1976.
4. Novel, C.P.E.R.E., *The epidemiological characteristics of an outbreak of 2019 novel coronavirus diseases (COVID-19) in China.* Zhonghua liu xing bing xue za zhi= Zhonghua liuxingbingxue zazhi, 2020. **41**(2): p. 145.

5. Gorbalenya, A.E., *Severe acute respiratory syndrome-related coronavirus–The species and its viruses, a statement of the Coronavirus Study Group.* bioRxiv, 2020.
6. Dong, E., H. Du, and L. Gardner, *An interactive web-based dashboard to track COVID-19 in real time.* The Lancet infectious diseases, 2020. **20**(5): p. 533-534.
7. Pedersen, N.C., *An update on feline infectious peritonitis: virology and immunopathogenesis.* The Veterinary Journal, 2014. **201**(2): p. 123-132.
8. Vlasova, A., et al., *Porcine coronaviruses*, in *Emerging and Transboundary Animal Viruses*. 2020, Springer. p. 79-110.
9. Snijder, E.J., E. Decroly, and J. Ziebuhr, *The Nonstructural Proteins Directing Coronavirus RNA Synthesis and Processing.* Adv Virus Res, 2016. **96**: p. 59-126.
10. van Hemert, M.J., et al., *SARS-coronavirus replication/transcription complexes are membrane-protected and need a host factor for activity in vitro.* PLoS Pathog, 2008. **4**(5): p. e1000054.
11. Shannon, A., et al., *Favipiravir strikes the SARS-CoV-2 at its Achilles heel, the RNA polymerase.* bioRxiv, 2020.
12. Subissi, L., et al., *One severe acute respiratory syndrome coronavirus protein complex integrates processive RNA polymerase and exonuclease activities.* Proceedings of the National Academy of Sciences of the United States of America, 2014. **111**(37): p. E3900-E3909.
13. Kirchdoerfer, R.N. and A.B. Ward, *Structure of the SARS-CoV nsp12 polymerase bound to nsp7 and nsp8 co-factors.* Nat Commun, 2019. **10**(1): p. 2342.
14. Gao, Y., et al., *Structure of the RNA-dependent RNA polymerase from COVID-19 virus.* Science, 2020. **368**(6492): p. 779-782.
15. Peng, Q., et al., *Structural and Biochemical Characterization of the nsp12-nsp7-nsp8 Core Polymerase Complex from SARS-CoV-2.* Cell Reports, 2020. **31**(11): p. 107774.
16. Hillen, H.S., et al., *Structure of replicating SARS-CoV-2 polymerase.* bioRxiv, 2020.
17. Ferron, F., et al., *Structural and molecular basis of mismatch correction and ribavirin excision from coronavirus RNA.* Proceedings of the National Academy of Sciences, 2018. **115**(2): p. E162-E171.
18. Gordon, C.J., et al., *The antiviral compound remdesivir potently inhibits RNA-dependent RNA polymerase from Middle East respiratory syndrome coronavirus.* J Biol Chem, 2020. **295**(15): p. 4773-4779.
19. Krichel, B., et al., *Processing of the SARS-CoV pp1a/ab nsp7-10 region.* Biochem J, 2020.
20. Zhai, Y., et al., *Insights into SARS-CoV transcription and replication from the structure of the nsp7-nsp8 hexadecamer.* Nat Struct Mol Biol, 2005. **12**(11): p. 980-6.
21. Xiao, Y., et al., *Nonstructural proteins 7 and 8 of feline coronavirus form a 2:1 heterotrimer that exhibits primer-independent RNA polymerase activity.* J Virol, 2012. **86**(8): p. 4444-54.
22. Li, S., et al., *New nsp8 isoform suggests mechanism for tuning viral RNA synthesis.* Protein Cell, 2010. **1**(2): p. 198-204.
23. Konkolova, E., et al., *Structural analysis of the putative SARS-CoV-2 primase complex.* Journal of Structural Biology, 2020. **211**(2): p. 107548.
24. Dülfer, J., et al., *Structural mass spectrometry goes viral.* Advances in virus research, 2019. **105**: p. 189-238.
25. Erba, E., L. Signor, and C. Petosa, *Exploring the structure and dynamics of macromolecular complexes by native mass spectrometry.* Journal of Proteomics, 2020: p. 103799.

26. Wang, G., A.J. Johnson, and I.A. Kaltashov, *Evaluation of electrospray ionization mass spectrometry as a tool for characterization of small soluble protein aggregates.* Analytical chemistry, 2012. **84**(3): p. 1718-1724.
27. Ziebuhr, J., *The coronavirus replicase*, in *Coronavirus replication and reverse genetics*. 2005, Springer. p. 57-94.
28. Hegyi, A. and J. Ziebuhr, *Conservation of substrate specificities among coronavirus main proteases.* J Gen Virol, 2002. **83**(Pt 3): p. 595-9.
29. Chen, J., et al., *Structural basis for helicase-polymerase coupling in the SARS-CoV-2 replication-transcription complex.* Cell, 2020.
30. Akabayov, B., et al., *Impact of macromolecular crowding on DNA replication.* Nature communications, 2013. **4**(1): p. 1-10.
31. Von Brunn, A., et al., *Analysis of intraviral protein-protein interactions of the SARS coronavirus ORFeome.* PloS one, 2007. **2**(5): p. e459.
32. Falke, S., *(Doctoral Thesis) Coronaviral Polyprotein Nsp7-10 : Proteolytic Processing and Dynamic Interactions within the Transcriptase/Replicase Complex*. 2014, Staats- und Universitätsbibliothek Hamburg.
33. Xue, X., et al., *Production of authentic SARS-CoV M pro with enhanced activity: application as a novel tag-cleavage endopeptidase for protein overproduction.* Journal of molecular biology, 2007. **366**(3): p. 965-975.
34. van den Heuvel, R.H., et al., *Improving the performance of a quadrupole time-of-flight instrument for macromolecular mass spectrometry.* Anal Chem, 2006. **78**(21): p. 7473-83.
35. Marty, M.T., et al., *Bayesian deconvolution of mass and ion mobility spectra: from binary interactions to polydisperse ensembles.* Analytical chemistry, 2015. **87**(8): p. 4370-4376.
36. Strohalm, M., et al., *mMass data miner: an open source alternative for mass spectrometric data analysis.* Rapid Communications in Mass Spectrometry: An International Journal Devoted to the Rapid Dissemination of Up-to-the-Minute Research in Mass Spectrometry, 2008. **22**(6): p. 905-908.
37. Franke, D., C.M. Jeffries, and D.I. Svergun, *Correlation Map, a goodness-of-fit test for one-dimensional X-ray scattering spectra.* Nature methods, 2015. **12**(5): p. 419.
38. Franke, D., A.G. Kikhney, and D.I. Svergun, *Automated acquisition and analysis of small angle X-ray scattering data.* Nuclear Instruments and Methods in Physics Research Section A: Accelerators, Spectrometers, Detectors and Associated Equipment, 2012. **689**: p. 52-59.
39. Hajizadeh, N.R., et al., *Consensus Bayesian assessment of protein molecular mass from solution X-ray scattering data.* Scientific reports, 2018. **8**(1): p. 1-13.
40. Svergun, D., C. Barberato, and M.H. Koch, *CRYSOL–a program to evaluate X-ray solution scattering of biological macromolecules from atomic coordinates.* Journal of applied crystallography, 1995. **28**(6): p. 768-773.
41. Konarev, P.V., et al., *PRIMUS: a Windows PC-based system for small-angle scattering data analysis.* Journal of applied crystallography, 2003. **36**(5): p. 1277-1282.
42. Petoukhov, M.V., et al., *New developments in the ATSAS program package for small-angle scattering data analysis.* Journal of applied crystallography, 2012. **45**(2): p. 342-350.
43. Sievers, F., et al., *Fast, scalable generation of high-quality protein multiple sequence alignments using Clustal Omega.* Molecular systems biology, 2011. **7**(1): p. 539.
44. Robert, X. and P. Gouet, *Deciphering key features in protein structures with the new ENDscript server.* Nucleic acids research, 2014. **42**(W1): p. W320-W324.

45. Goddard, T.D., et al., *UCSF ChimeraX: Meeting modern challenges in visualization and analysis.* Protein Science, 2018. **27**(1): p. 14-25.